

# A Deep *Hubble Space Telescope* H-Band Imaging Survey of Massive Gas-Rich Mergers. II. The QUEST QSOs <sup>1</sup>

S. Veilleux<sup>2</sup>, D.-C. Kim<sup>3</sup> and D. S. N. Rupke<sup>4</sup>

*Department of Astronomy, University of Maryland, College Park, MD 20742;*  
*veilleux@astro.umd.edu, ddk3wc@mail.astro.virginia.edu, drupke@ifa.hawaii.edu*

C. Y. Peng

*Herzberg Institute of Astrophysics, National Research Council of Canada, 5071 West Saanich Rd., Victoria, BC V9E 2E7, Canada; cyp@nrc-cnrc.gc.ca*

L. J. Tacconi, R. Genzel, D. Lutz, E. Sturm, A. Contursi, and M. Schweitzer

*Max-Planck-Institut für extraterrestrische Physik, Postfach 1312, D-85741 Garching, Germany; linda@mpe.mpg.de, genzel@mpe.mpg.de, lutz@mpe.mpg.de, sturm@mpe.mpg.de, contursi@mpe.mpg.de, schweitzer@mpe.mpg.de*

K. M. Dasyra

*Spitzer Science Center, Mail Code 220-6, California Institute of Technology, 1200 East California Boulevard, Pasadena, CA 91125; dasyra@ipac.caltech.edu*

L. C. Ho

*The Observatories of the Carnegie Institution of Washington, 813 Santa Barbara St., Pasadena, CA 91101; lho@ociw.edu*

D. B. Sanders

*Institute for Astronomy, University of Hawaii, 2680 Woodlawn Drive, Honolulu, HI 96822; sanders@ifa.hawaii.edu*

A. Burkert

*University Observatory Munich, Scheinerstrasse 1, D-81679 Munich, Germany; burkert@usm.uni-muenchen.de*

## ABSTRACT

We report the results from a deep *HST* NICMOS H-band imaging survey of 28  $z < 0.3$  QSOs from the Palomar-Green (PG) sample. This program is

part of *QUEST* (*Quasar / ULIRG Evolution Study*) and complements a similar set of data on 26 highly-nucleated ULIRGs presented in Paper I. Our analysis indicates that the fraction of QSOs with elliptical hosts is higher among QSOs with undetected far-infrared (FIR) emission, small infrared excess ( $L_{\text{IR}}/L_{\text{B}} < 10$ ), and luminous hosts. The hosts of FIR-faint QSOs show a tendency to have less pronounced merger-induced morphological anomalies and larger QSO-to-host luminosity ratios on average than the hosts of FIR-bright QSOs, consistent with late-merger evolution from FIR-bright to FIR-faint QSOs. The spheroid sizes ( $\sim 0.3 - 5.5$  kpc) and total host luminosities ( $\sim 0.6 - 7.2 L_H^*$ ) of the radio-quiet PG QSOs in our sample are statistically indistinguishable from the ULIRG hosts presented in Paper I, while those of radio-loud PG QSOs are systematically larger and more luminous. ULIRGs and PG QSOs with elliptical hosts fall near, but not exactly on, the fundamental plane of inactive spheroids. We confirm the systematic trend noted in Paper I for objects with small ( $\lesssim 2$  kpc) spheroids to be up to  $\sim 1$  mag. brighter than inactive spheroids. The host colors and wavelength dependence of their sizes support the idea that these deviations are due at least in part to non-nuclear star formation. However, the amplitudes of these deviations depend mainly on host sizes, and possibly on infrared excess, but not on merger phase, QSO-to-host luminosity ratio, optical spectral type, AGN fractional contribution to the bolometric luminosity, or host R–H color. Taken at face value (i.e., no correction for extinction or the presence of a young stellar population), the H-band spheroid-host luminosities imply black hole masses  $\sim 5 - 200 \times 10^7 M_\odot$  and sub-Eddington mass accretion rates for both QSOs and ULIRGs. These results are compared with published black hole mass estimates derived from other methods.

*Subject headings:* galaxies: active – galaxies: interactions – galaxies: quasar – galaxies: starburst – infrared: galaxies

---

<sup>1</sup>Based on observations with the NASA/ESA *Hubble Space Telescope*, obtained at the Space Telescope Science Institute, which is operated by the Association of Universities for Research in Astronomy, Inc. under NASA contract No. NAS5-26555.

<sup>2</sup>Also: Max-Planck-Institut für extraterrestrische Physik, Postfach 1312, D-85741 Garching, Germany

<sup>3</sup>New address: Department of Astronomy, University of Virginia, Charlottesville, VA 22904-4325

<sup>4</sup>New address: Institute for Astronomy, University of Hawaii, 2680 Woodlawn Drive, Honolulu, HI 96822.

## 1. Introduction

In this series of papers, the structural properties of massive gas-rich mergers in the local universe are derived to provide insights into galaxy merging, a key driving force of galaxy evolution over the history of the universe. This study is part of a comprehensive program called QUEST - Quasar/ULIRG Evolution Study. This program combines optical and near-infrared imaging and spectroscopic data obtained from the ground with H-band imaging and mid-infrared spectroscopic data obtained with the *Hubble Space Telescope (HST)* and *Spitzer Space Telescope*, respectively (see Veilleux et al. 2009 and references therein, for a more detailed discussion of QUEST).

In Veilleux et al. (2006; hereafter Paper I), we reported the results from a Cycle 12 *HST* NICMOS H-band imaging survey of 26  $z < 0.3$  ULIRGs and 7 infrared-bright Palomar-Green (PG) QSOs. Unsuspected double nuclei were detected in 5 ULIRGs. The great majority (81%) of the single-nucleus systems showed a prominent elliptical-like morphology. However, low-surface-brightness exponential disks were detected on large scale in at least 4 of these sources. The hosts of ‘warm’ (*IRAS* 25-to-60  $\mu\text{m}$  flux ratio,  $f_{25}/f_{60} > 0.2$ ), AGN-like systems were found to be elliptical-like and have less pronounced merger-induced morphological anomalies than the hosts of cool systems with LINER or HII region-like nuclear optical spectral types, suggestive of merger-driven evolution from cool to warm ULIRGs. The host sizes and luminosities of the 7 PG QSOs in the sample were statistically indistinguishable from those of the ULIRG hosts. The hosts of ULIRGs and PG QSOs were found to lie close to the locations of intermediate-luminosity ( $\sim 0.5 - 2 L^*$ ) spheroids in the photometric projection of the fundamental plane (FP) of ellipticals. However, ULIRGs with small hosts were found to be generally brighter than normal inactive spheroids, possibly due to excess near-infrared emission from a circumnuclear starburst.

The 7 PG QSOs in the Cycle 12 sample were selected to be far-infrared (FIR) brighter than typical PG QSOs. Netzer et al. (2007) have recently argued that the bulk of the infrared luminosity,  $L_{\text{IR}} \equiv L(8 - 1000\mu\text{m})$ , in PG QSOs is produced by a massive starburst. So it is not clear whether the Cycle 12 results can be generalized to PG QSOs as a whole. Here we report the results from an analysis of 21 additional PG QSOs to address this issue. In Section 2, we describe the sample of QSOs used in our study along the extensive ancillary dataset on these objects. Our methods to obtain, reduce, and analyze the data are very similar to those used in Paper I, so we discuss them only briefly in Section 3. The results are presented in Section 4 and discussed and compared with those of earlier studies in Section 5. The main conclusions are summarized in Section 6. Throughout this paper, we adopt  $H_0 = 75 \text{ km s}^{-1} \text{ Mpc}^{-1}$ ,  $\Omega_M = 0.3$ , and  $\Omega_\Lambda = 0.7$ .

## 2. QSO Sample & Ancillary Data

The QSO component of QUEST has already been discussed in detail in Schweitzer et al. (2006, 2008), Netzer et al. (2007), and Veilleux et al. (2009) and this detailed discussion will not be repeated here. The Cycle 15 *HST* sample consists of 23  $z \lesssim 0.3$  quasars, including 22 Palomar-Green (PG) quasars from the Bright Quasar Sample (Schmidt & Green 1983) and another one (B2 2201+31A = 4C 31.63) with a  $B$  magnitude that actually satisfies the PG QSO completeness criterion of Schmidt & Green (1983). Failure to acquire guide stars with the Fine Guidance Sensors severely degraded the observations for two of these objects (PG 0953+414 and PG 1004+130), so they are not discussed any further in the paper.

The combined sample of 28 PG QSOs successfully observed during Cycles 12 and 15 covers the low-redshift and low B-band luminosity ends of the PG QSO sample (see Figure 2 in Veilleux et al. 2009), and they are well matched in redshift with the 1-Jy ULIRGs studied in Paper I (Figure 3 of Veilleux et al. 2009). The combined sample of QSOs is representative of the entire PG QSO sample in terms of infrared excess (i.e., the infrared-to-blue luminosity ratio,  $L_{IR}/L_B$ ), and FIR brightness [ $L(60 \mu\text{m})/L(15 \mu\text{m})$ , Netzer et al. 2007]. Table 1 lists some of the properties of the QSOs in our study, including those observed during Cycle 12. Note that three of the QSOs in the *HST* sample (PG 1119+120, 1126–041, and 1229+204) have absolute B-band magnitudes which are fainter than the traditional luminosity threshold of QSOs ( $M_B = -23$  for  $H_0 = 50 \text{ km s}^{-1} \text{ Mpc}^{-1}$  and  $q_0 = 0$  or  $M_B = -22.3$  for the cosmology adopted here).

An extensive set of data already exists on these objects. Ground-based optical and near-infrared images of many of these objects have been obtained in tip-tilt mode (Surace et al. 2001) and adaptive-optics mode (Guyon et al. 2006), providing a spatial resolution of  $0''.2 - 0''.8$  and  $0''.13-0''.30$ , respectively, i.e., only slightly poorer than that of the *HST* data presented here ( $\sim 0''.14$ ). However, a key advantage of the present data over previous data sets is the stability of the *HST* point-spread function, which allows us to derive reliable structural parameters of the QSO hosts well within  $1''$  of the center. Archival optical *HST* images of several local type 1 AGN, including some from the present sample, were recently analyzed by two in our group (C.Y.P., L.C.H.) and published as Kim et al. (2008a), and also independently studied by Hamilton et al. (2008). The results from these previous studies are compared with those from our *HST* survey in Sections 4 and 5. All of these QSOs have also been studied spectroscopically at optical wavelengths from the ground (Boroson & Green 1992) and in the mid-infrared with *Spitzer* (Schweitzer et al. 2006, 2008; Netzer et al. 2007; Veilleux et al. 2009). This last dataset provides valuable information on the AGN contribution to the bolometric luminosities of these objects; we make use of this information in Section 5. In addition, VLT/Keck near-infrared spectroscopic data exist for a number of

these objects. Dynamical estimates of the masses of the hosts were derived from these data (Dasyra et al. 2007) and are compared with our photometric estimates in Section 5.

### 3. Data Acquisition, Reduction, and Analysis

The methods used to acquire, reduce and analyze the present data are nearly identical to those of Paper I, so only a summary is given below; interested readers should refer to Paper I for more detail.

The main driver of our Cycle 15 program on the QSOs was to match the observational setup (instrument, filter, detection level, dither pattern) used for our Cycle-12 data to facilitate comparisons between the two datasets. Our Cycle-12 results have confirmed that the excellent spatial resolution and sensitivity of *HST* NICMOS in the non-thermal infrared are required to extract the central point sources from our targets and derive accurate structural parameters on the hosts. NICMOS is better suited for this program than ACS to reduce the impact of dust extinction and star formation on the measurements (especially in the cores of ULIRGs and infrared bright QSOs) and to exploit the contrast between QSO and elliptical hosts (e.g., McLeod & McLeod 2001 and references therein). The strong thermal background makes deep observations at K unrealistic; our program therefore focuses on the H band, roughly matching the waveband of our VLT and Keck spectra. The need for *deep* images can hardly be overstated. Comparisons of our Cycle-12 data with the results derived from shallow (e.g., SNAP) HST images from the archives show that the shallow HST data underestimate the luminosities and half-light radii of the hosts, make profile fitting ambiguous (e.g., Sérsic spheroid versus exponential disk), and can even completely overlook low surface brightness, tidal distortions or exponential disks extending significantly beyond galactic bulges. To avoid these problems, we tried to match the detection level ( $S/N \approx 3$ ) of our Cycle-12 data ( $\sim 22.0$  H mag. arcsec $^{-2}$ ) by observing each target for one full orbit (on-target exposure time of 2650 seconds).

NIC2 was selected for our Cycle 15 program, based on the requirements of good sensitivity to low surface brightness features, excellent spatial resolution ( $0''.076$  pixel $^{-1}$ ) for accurate PSF (FWHM =  $0''.14$ ) removal, and a field of view ( $19''.5 \times 19''.5$ ) large enough to encompass most of the structures in our targets. To help with the PSF subtraction, we also requested an additional orbit to obtain a deep exposure of a star (SA 107-626) and fully characterize the PSF at H.

Given the redshifts of our targets ( $z \sim 0.05 - 0.33$ ; Table 1) and the strengths of the emission features in ULIRGs and QSOs (see, e.g., Veilleux et al. 1997, 1999; Dasyra et al.

2007), contamination by emission lines (e.g., [Fe II]  $\lambda$ 1.644, Pa $\beta$ ) is at most  $\sim 10\%$  for the F160W filter, and is therefore not an issue here. We used the logarithmic MULTIACCUM sequences to provide the largest dynamic range and allow the calibration software to recover the bright central point source. The telescope was dithered between exposures to better sample the instrumental PSF, and to aid with the recognition and elimination of data artifacts.

The raw *HST* NICMOS data were first processed with the IDL procedure *undopuft.pro* written by Eddie Bergeron at STScI (Space Telescope Science Institute) to remove the electronic echoes of bright sources and associated stripes, and subsequently processed with the standard pipeline processing task *calnica* within IRAF/STSDAS to correct for nonlinearity of the detector and removes bias value, dark current, amplifier glow, and shading. The IDL procedure *saa\_clean.pro* was used to remove the effects of cosmic ray persistence (Bergeron & Dickinson 2003). Next, the four dithered exposures of each object were combined using the “drizzle” technique (Gonzaga et al. 1998). For the photometric calibration of the reduced data, a Vega-normalized magnitude for F160W (NIC2) was derived following the recipe in the *HST* Data Handbook for NICMOS (Dickinson et al. 2002) using the calibration appropriate for Cycle 15.

The two-dimensional fitting algorithm GALFIT (Peng et al. 2002) was used to accurately remove the central point source in each object and determine the structural parameters of the underlying host. In some cases, the analysis was carried out a second time by other members of our group to independently verify the significance of the results. The analysis of each object followed a number of well-defined steps. First, we constructed a mask to exclude bright stars or small foreground/background galaxies within the field of view. Next, we proceeded to fit the surface brightness distribution of each object using a single Sérsic component (observed intensity profile  $I \propto \exp[-R^{1/n}]$ ) to simulate the galaxy host and a PSF model to account for the possibility of an unresolved nuclear starburst or AGN. The high-S/N PSF model was derived from our deep images of SA 107-626. The Sérsic component was convolved with the PSF before comparison with the data. Three Sérsic components were examined:  $n = \text{free}$  (i.e., left unconstrained),  $n = 1$  (exponential disk profile), and  $n = 4$  (de Vaucouleurs profile). In all cases, the centroids of the PSF and Sérsic components were left unconstrained. This relatively simple one galaxy component analysis allowed us to get a general sense of the complexity of each system and whether the system is disk- or spheroid-dominated.

As was the case for the ULIRGs and infrared-bright QSOs in Paper I, the residuals from the one component galaxy fit to the QSOs are often quite significant. This is generally the results of merger-induced morphological anomalies. However, in other cases, these

residuals may indicate the presence of a second low-surface-brightness galaxy component (e.g., disk). So we decided to look into this possibility by adding a second (PSF-convolved) galaxy component to the fits for each object and examining the effects on the goodness of the fits. To limit our search, we only studied the ( $n = 1$ ) + ( $n = 4$ ) case. Here again, the centroids of the various components were left unconstrained. Not surprisingly given the larger number of free parameters, these two-component models generally provide better fits to the data. However, a careful examination of the fitted components often indicate that the second galaxy component is not physically meaningful (see list of telltale signs in Section 5.2 of Paper I). The surest way to recognize when a second galaxy component is real is to “put back” into the residual image the model components individually to see which structure was being fitted. The components have to be fairly distinct both spatially (e.g. axis ratio, size, centering) and morphologically (concentration) for us to accept the two components as being real in our assessment.

This procedure provided reliable host-galaxy structural parameters for all but 3 objects in our sample (see Section 4.1 for a discussion of the measurement uncertainties). For PG 1116+215, PG 1617+175, and PG 2251+113, significant residuals due to PSF mismatches were found near the cores of these objects. The structural parameters derived for these objects are considered unreliable and not included in our search for trends (Section 4) and discussion (Section 5).

## 4. Results

### 4.1. General Considerations & Uncertainties

The main results from the GALFIT analysis are shown in Figures 1 and 2 and listed in Tables 2 – 5 (readers who are looking for a quick summary of the results should refer to Table 5). Figure 1 presents the residuals found after subtracting one galaxy component models (PSF + Sérsic with  $n =$  free, 1, or 4) from the surface brightness distributions of single-nucleus systems in our sample. In several cases, we find that adding another Sérsic component significantly improves the goodness of the fits; the results of this more sophisticated two galaxy component analysis are shown in Figure 2. The structural parameters derived from the one and two galaxy component fits are listed in Tables 2 and 3, respectively. Note that the exact value of  $n > 4$  is not too significant. It generally indicates the galaxy has either a strong core (e.g., bulge dominated) or an extended wing (e.g. elliptical galaxies or interacting/neighbors galaxies), or both. Large  $n$  can be caused by bad AGN subtraction, but we tried to minimize that likelihood by using multiple components for the core. We also tried to minimize neighboring contamination by fitting the neighbors and/or masking.

Indeed, our images often show small galaxies in the vicinity of the PG QSOs, but they are considerably fainter ( $\Delta m_H \gtrsim 4$  mags) than the QSO hosts. We have no data to determine if these small objects are associated or not with the QSOs, so we list the magnitudes of the objects in a separate table, Table 4, but do not discuss them any further in this paper.

Table 5 provides a summary of the best-fitting model for each object in the sample along with a visual (hence subjective) assessment of the presence of a stellar bar, spiral arms, and strong merger-induced disturbances. The best-fitting models listed in this table were adopted by inspecting the residuals in Figures 1 and 2 and the reduced chi-squares,  $\chi_\nu^2$ , listed in Tables 2 and 3. The first of these  $\chi_\nu^2$  values takes into account residuals over the entire galaxy whereas the second one excludes the central portion which is affected by errors in the subtraction of the central PSF. These reduced chi-squares values should be used with caution when choosing the best fits. First, we note that they are generally significantly larger than unity so the fits are not formally very good. This is due in large part to the presence of merger-induced morphological anomalies; we return to this important point below (Section 4.3). We also notice that the chi-squares tend to be higher for larger, brighter, and more PSF-dominated objects. This is not unexpected given the definition of  $\chi_\nu^2$ , which is not normalized by the intensity, and given that the fraction of the detector area that is free of galaxy emission is more limited for large systems than for small ones. Thus,  $\chi_\nu^2$  cannot be used to compare the goodness of fits between objects. However, it is a useful quantity to compare the quality of fits for the same object (the interested readers should refer to Sections 5 and 6 of Paper I for a more detailed discussion of the factors involved in our morphological classification).

The NIC2 observations of the QUEST sample have very high signal-to-noise, therefore the uncertainties in the fit parameters are generally dominated by systematic errors rather than random errors due to Poisson noise. Systematic errors come about from several factors, the most common ones being a mismatch in the PSF between the data and the model, a mismatch between the galaxy profile with the model assumptions, or when the sky background cannot be determined accurately for various reasons. Even though the errors are systematic, in AGN studies where PSF mismatch is great, there is some randomness involved in the sense that different PSF choices we make are drawn from a distribution around some average PSF shape. In high signal-to-noise, the amount of systematic error depends on the luminosity contrast between the host galaxy and the AGN component. The typical contrast in the QUEST sample of AGN-to-host luminosity (Table 5, Col. 6) ranges mostly between 1 and 5, with a median of 1.5.

Kim et al. (2008b) performed very detailed AGN image fitting simulations which can be used to estimate the uncertainty in the fitting parameters. Their study quantified the degree



of measurement uncertainty by drawing on different PSFs. The scatter and systematic errors are also presented as a function of signal-to-noise, AGN-to-host contrast, and the size of the host galaxy, due to different PSF choices. Therefore we mostly draw upon that study to infer that the systematic uncertainty for the QUEST sample to be about 10% for the host galaxy luminosity. The random uncertainty due to our ignorance about the PSF are roughly: 20-50% for the effective radius,  $\sim 15\%$  for the host galaxy luminosity, and  $< 10\%$  for the AGN luminosity. We can also empirically quantify the uncertainty in the host luminosity Columns 4 (host luminosity including tidal features) and 5 (model host luminosity) in Table 5, from which we obtain an uncertainty of roughly  $\lesssim 15\%$ .

Note that the host galaxies of PG0050+124, PG0838+770, PG1229+204, PG1426+015, and PG2214+139 cover a significant fraction of the field of view of NIC2. The sky background is therefore difficult to determine accurately in these images and the structural parameters of these objects are more uncertain. This is noted in Tables 2, 3, and 5.

## 4.2. Morphological Type of Host Galaxy

The one galaxy component analysis indicates that a single spheroidal component often provides a good fit to the surface brightness distribution of the central portion of the PG QSO hosts. However, the excellent sensitivity limit of our data allows us to also detect the presence of faint, low-surface-brightness disks in 9/28 (32%) objects. The results of our attempts to fit this second component as an exponential disk are listed in Table 3 and shown in Figure 2. Table 5 only lists the results for those nine cases where the addition of a second,  $n = 1$  component improved the fit significantly and the result was physically meaningful (e.g., the disk had to be concentric with, and larger than, the bulge). Note that stellar bars are present in at least two of these QSOs (PG 0838+770 and PG 1229+204; already pointed out by Surace et al. 2001). A stellar bar may also be present in the elliptical host of PG 1001+054, but the presence of small-scale features in this last object limits the analysis.

Trends are seen between morphological classification and infrared properties. QSOs with elliptical hosts have slightly smaller infrared excesses (Figure 3d). The median  $L_{\text{IR}}/L_{\text{B}}$  ratio among elliptical, bulge + disk, ambiguous hosts is 8.5, 10.5, and 10.4, respectively. This trend fits naturally with the results of Paper I, where we found that ULIRGs with warm 25-to-60  $\mu\text{m}$  ratios, small infrared excesses, and optical Seyfert characteristics tend to have elliptical hosts (Figures 3a and 3b). This trend is also consistent with, although weaker than, that from the study of Guyon et al. (2006).

Interestingly, QSOs with elliptical hosts do *not* have larger 25-to-60  $\mu\text{m}$  ratios than

those with bulge + disk or ambiguous hosts (Figure 3c, median ratios of 0.32, 0.50, and 0.41, respectively). So it appears that the trend seen in Paper I between this ratio and the morphological classification of ULIRGs breaks down at the smaller infrared excesses of typical QSOs.

We also note in Figure 3e that all FIR-undetected QSOs have elliptical hosts. But this may be due to the fact that most of these QSOs are also bolometrically luminous. Indeed, we find that the more luminous QSOs in our sample favor elliptical hosts over late-type hosts (Figure 3f). Three of the five radio-loud QSOs in our sample have elliptical hosts. These results bring further support for a luminosity and radio-loudness dependence of the host morphological type among QSOs (e.g., Dunlop et al. 2003, Guyon et al. 2006, Paper I; Best et al. 2007; Wolf & Sheinis 2008 and references therein; see also Section 5.1 below).

### 4.3. Strength of Tidal Features

Signs of galactic interactions such as tidal tails and bridges, lopsided disks, distorted outer isophotes, or double nuclei are visible in the majority (16/28 = 57%) of the QSOs (and in all ULIRGs, Paper I). The residual maps in Figures 1 and 2 are a particularly good indicator of these tidal features. Following Paper I, we quantified the importance of these features by first adding up the absolute values of the residuals from the best one or two galaxy component fits over the region unaffected by the PSF subtraction and then normalizing this quantity to the total host luminosities (including tidal features); the results are listed in column (11) of Tables 2 and 3. Although this quantity is sensitive to the presence of spiral structure, dust lanes, and bright star clusters, we find in our objects that  $R_2$  is dominated by the presence of large-scale merger-induced anomalies.

In Figure 4a and 4b, we plot  $R_2$  versus the *IRAS* 25-to-60  $\mu\text{m}$  colors for all QSOs and ULIRGs in our sample. PG QSOs and warm quasar-like ULIRGs systems tend to have smaller residuals than the other objects in the sample. All PG QSOs and Seyfert ULIRGs have  $R_2 < 30\%$ . In Paper I, we found that ULIRGs with late-type or ambiguous morphologies show larger residuals than elliptical systems (Figure 5b), suggesting that galaxies with a prominent spheroid are in the later stages of a merger than the late-type and ambiguous systems. Our new data on the PG QSOs do show a similar difference between elliptical and ambiguous systems (the residuals from the two galaxy component fits are expected to be smaller than those from the one galaxy component fits, so the bulge + disk systems are not considered in our discussion).

In Figures 4c and 4d, we compare the fit residuals with the magnitude of the infrared

excess as a function of morphological classification and FIR strength, respectively. We find a slight trend of increasing residuals with increasing infrared excess and FIR strength, indicating that stronger merger-induced morphological disturbances are found among FIR-bright QSOs with large infrared excesses, as was suggested by Guyon et al. (2006). The FIR emission in QSOs is now believed to be primarily associated with starburst activity (Netzer et al. 2007), so this result indicates that starburst activity declines during the final phases of the merger process, consistent with recent numerical simulations of major equal-mass ( $\sim 1:1$ ) mergers (e.g., Johansson et al. 2009). Note that the presence of discernible disks in several low-luminosity PG QSOs can also be explained in the major merger scenario if significant re-accretion of residual cold gas formed these disks (e.g., Governato et al. 2008). In these systems, local processes such as gas inflows along nuclear bars or spiral arms may also be contributing to the feeding of the AGN (e.g., Storchi-Bergmann et al. 2007 and references therein).

#### 4.4. Strength of Unresolved Nucleus

Following Paper I, we quantified the importance of the PSF by calculating the flux ratio of the PSF to the host,  $I_{\text{PSF}}/I_{\text{host}}$  using the best one or two galaxy component model for each object. In Paper I, we found that this ratio is less than unity for all ULIRGs, except for all 5 ULIRGs optically classified as Seyfert 1s. Figure 5a shows that most PG QSOs have PSF-to-host ratios above unity, indistinguishable from those of Seyfert 1 ULIRGs. The PG QSOs strengthen the positive correlation noted in Paper I between the PSF-to-host ratio and *IRAS* 25-to-60  $\mu\text{m}$  color. The AGN therefore dominates the central H-band emission in Seyfert 1 ULIRGs and QSOs. As noted in Paper I, this result does not rule out the possibility that a nuclear starburst is also contributing to the PSF emission, but this starburst does not produce the bulk of the H-band emission in the nucleus of these objects. This is consistent with the strong dilution of the CO bandheads observed in the near-infrared spectra of Seyfert 1 ULIRGs and PG QSOs of Dasyra et al. (2007).

A slight trend is also seen between PSF-to-host ratios and infrared excesses (or FIR brightnesses) among QSOs: those with large infrared excesses tend to have smaller PSF-to-host ratios (Figure 5b). This is consistent with the merger scenario if FIR-bright QSOs represent an earlier phase of QSO/merger evolution when the QSOs have not fully emerged from their dusty cocoons.

#### 4.5. Host Sizes, Magnitudes, and Colors

Figure 6 shows the distributions of host sizes (spheroid component only) and total (spheroid + tidal features + disk, if relevant) host absolute magnitudes for all ULIRGs and PG QSOs in the *HST* sample. The full range in QSO spheroid half-light radii and total host luminosities is very broad, from  $r_{\frac{1}{2}} = 0.3$  to 9.9 kpc and from  $M_H = -23.19$  to  $-26.08$  or  $\sim 0.6 - 9.0 L_H^*$ , respectively (we used  $M_H^* = -23.7$  mag. as the H-band absolute magnitude of a  $L^*$  galaxy in a Schechter function description of the local field galaxy luminosity function; Cole et al. 2001; Veilleux et al. 2006). The average (median) spheroid half-light radii and total H-band absolute magnitudes of the QSO hosts in the sample are  $2.87 \pm 2.59$  (2.14) kpc and  $-24.60 \pm 0.77$  ( $-24.46$ ) mag. For comparison, the same quantities for the ULIRGs in Paper I are  $2.55 \pm 1.43$  (1.84) kpc and  $-24.06 \pm 0.56$  ( $-24.21$ ) mag. These average QSO and ULIRG host magnitudes correspond to  $\sim 2.3 \pm 1$  and  $\sim 1.5 \pm 1 L_H^*$ , respectively.

A Kolmogorov-Smirnov (K-S) analysis shows that the hosts of the PG QSOs in our sample are statistically different from the hosts of the 1-Jy ULIRGs in terms of absolute magnitudes but not in terms of sizes [P(null) = 2.2% and 59%, respectively]. A closer look at Figures 6a and 6b shows that the difference comes entirely from the inclusion of radio-loud QSOs in our sample. The hosts of these systems are systematically larger and brighter than those of the radio-quiet QSOs in our sample ( $r_{\frac{1}{2}} = 3.0$  to 9.9 kpc and from  $M_H = -24.11$  to  $-26.08$  or  $\sim 1 - 9 L_H^*$  versus  $r_{\frac{1}{2}} = 0.3$  to 5.5 kpc and from  $M_H = -23.19$  to  $-25.84$  or  $\sim 0.6 - 7.2 L_H^*$ ). Similar differences have been found in the past (e.g., Dunlop et al. 2003; Guyon et al. 2006; Best et al. 2007; Wolf & Sheinis 2008 and references therein). Figure 6b also shows that QSOs with elliptical hosts display the broadest range of luminosity, while the bulge + disk systems and the ambiguous systems tend to populate the low- and high-luminosity ends of the distribution, respectively.

We generally find good agreement on an object-by-object basis when comparing our host H-band magnitudes with those of McLeod & McLeod (2001; two objects in common), Surace et al. (2001; 8 objects), and Guyon et al. (2006; 20 objects). The comparisons with Surace et al. (2001) and Guyon et al. (2006) are shown in Figure 7. The Surace et al. host magnitudes plotted in Figure 7a were calculated by subtracting the nuclear magnitudes from the integrated magnitudes in their Table 2. An excellent match is found, except for one object, PG 0007+106, which is  $\sim 1$  mag. brighter in the Surace et al. data. This is an optically violently variable source so the difference may be due to uncertainties in the removal of the central PSF in the ground-based data. The Guyon et al. values tend to be  $\sim 0.4$  mag. brighter than our measurements. Given the good agreement between our data and those of Surace et al. and the noted variability of the PSF in the AO data of Guyon et al., we suspect that this shift is due to uncertainties in the PSF subtraction from these

latter data. Systematic underestimate of the background level in these latter data could also explain the shift.

There are 13 and 10 objects in common between the present H-band study and the archival optical *HST* imaging studies of Kim et al. (2008a) and Hamilton et al. (2008), respectively. The R-band (V-band) total host magnitudes of Kim et al. (Hamilton et al.) are compared with our H-band magnitudes in Figure 7c (7d). The average (median) R–H color derived from Figure 7c is  $1.80 \pm 0.53$  mag. (1.92 mag.). This median value is the same as that found by Jahnke et al. (2004) among 19 low-redshift ( $z < 0.2$ ) quasar host galaxies. It is  $\sim 0.3$  mag. bluer than the  $k$ -corrected R–H colors of elliptical galaxies with  $M_H \approx -24.5$  mag. at  $z \sim 0.2$  (Lilly & Longair 1984; Fukugita et al. 1995; Fioc & Rocca-Volmerange 1999; Jahnke et al. 2004; Hyvönen et al. 2007, 2008). Similarly, the median V–H color derived from Figure 7d is 1.9 mag., considerably bluer than the  $k$ -corrected V–H colors of elliptical galaxies with  $M_H \approx -24.5$  mag. at  $z \sim 0.2$  ( $V-H \approx 2.8$ ). A comparison of the half-light radii of the spheroidal components from the various data sets suggests a systematic difference between the near-infrared and optical measurements, where the H-band sizes are  $\sim 50\%$  smaller than the optical sizes, but the statistics are poor.

These shifts in colors and possibly sizes provide independent confirmation of the presence of a young circumnuclear stellar population in the hosts of many low- $z$  QSOs (e.g., Surace et al. 2001; Miller & Sheinis 2003; Canalizo et al. 2006, 2007; Schweitzer et al. 2006; Jahnke et al. 2004, 2007, and references therein). A young stellar population is a natural by-product of gas-rich galaxy mergers. One would therefore naively expect correlations between R–H and V–H colors and indicators of the merger phase, such as PSF-masked residuals, PSF-to-host ratios, infrared excesses, and FIR strength. No obvious trend is observed when combining ULIRGs and PG QSOs, but (1) the statistics are poor (the number of objects is never more than 11), (2) variations in the dust content and dust spatial distribution may be masking underlying correlations (this possible “cosmic conspiracy” between stellar evolution and extinction was also mentioned in Tacconi et al. 2002), and (3) the host colors exclude any emission from point-source nuclear starbursts since this nuclear emission was removed during the PSF subtraction procedure. So the host colors of these systems need not be correlated with the merger phase if the bulk of the emission from merger-induced star formation is in the nuclear regions (this is the case for most if not all ULIRGs, e.g., Soifer et al. 2000, and possibly also in some PG QSOs). These three factors may also explain the lack of any obvious color difference with morphological class or radio-loudness.

## 5. Discussion

In Paper I, we tried to answer two important questions: (1) are ULIRGs/QSOs elliptical galaxies in formation, and (2) are ULIRGs related to QSOs? Here, we revisit these questions following the same procedure as in Paper I, but this time the QSO population is better sampled by the new NICMOS data and near- and mid-infrared spectroscopic data recently published by our group are used to add important physical constraints on these objects. First, in Section 5.1, we use the FP traced by inactive spheroids to address these issues. Next, in Section 5.2, we characterize the black hole masses and level of black-hole driven activity likely to be taking place in the cores of these sources.

### 5.1. The Fundamental Plane

We focus our discussion on ULIRGs and QSOs with “pure” elliptical hosts, i.e., excluding the bulge + disk and ambiguous systems, to avoid uncertainties related to the bulge/disk decomposition (e.g., Kim et al. 2008a, 2008b) at the cost of reducing the sample size. Figure 8a shows that ULIRGs and QSOs with elliptical hosts lie near, but not exactly on, the photometric projection of the FP for spheroids as traced by the  $K'$ -band data of Pahre (1999, using  $H-K' = 0.35$  mag.), the  $z$ -band data of Bernardi et al. (2003; using  $z-H = 1.8$  mag.) and the H-band data of Zibetti et al. (2002). As found in Paper I, small ULIRG and QSO hosts are systematically brighter than inactive spheroids of the same size. The shift in surface brightness reaches  $\sim 1$  mag. for objects with half-light radii of  $\lesssim 1$  kpc. This systematic trend with half-light radii for both ULIRGs and PG QSOs is also seen in the linear fits through the data. The fits through the ULIRGs and PG QSOs (dashed and solid lines in Figure 8a, respectively) are indistinguishable from each other, but they are considerably steeper than the fit through the data of the inactive spheroids (dotted line). Interestingly, the K-band data of Rothberg & Joseph (2006) on optically-selected mergers (using  $H-K = 0.50$ ) show a similar shift at small half-light radii as that of our ULIRGs and PG QSOs. In Paper I, we speculated that the shift to brighter magnitudes among the small ULIRG/QSO hosts was due to excess H-band emission from a young stellar population, but did not have the relevant data to test this statement (see also discussion in Tacconi et al. 2002 and the relevant new results of Graves et al. 2009 and Hopkins et al. 2009 and Choi et al. 2009 on quiescent and UV-excess early-type galaxies, respectively). We now revisit this issue.

In Figure 8b, we combine the photometric measurements of Figure 8a with the stellar velocity dispersion measurements of Dasyra et al. (2006b, 2007) and Rothberg & Joseph (2006) and compare the results with the data on intermediate-size inactive spheroids from

Zibetti et al. (2002) and Bernardi et al. (2003). Here again, deviations are seen at small half-light radii in the sense that our ULIRGs and PG QSOs and the optically-selected mergers of Rothberg & Joseph (2006) fall systematically below the FP of inactive spheroids. This effect was noted by Rothberg & Joseph (2006) and attributed to differences in the effective radius and brighter surface brightness, rather than a lower velocity dispersion; this is consistent with the explanation of excess H-band emission from a young circumnuclear stellar population. Additional support for this idea comes from our result in Section 4.5 that the colors of the PG QSO hosts are bluer than those of inactive spheroids of similar size.

However, if we define “surface brightness deviation” as the difference between the observed surface brightness and the surface brightness expected of a inactive spheroidal galaxy with the same half-light radius, as determined by the linear fit through the data of Pahre (1999), Bernardi et al. (2003), and Zibetti et al. (2002) in Figure 8*a*, we find no obvious trend between surface brightness deviations and R–H host colors (derived by combining the data of Veilleux et al. 2002, 2006, Kim et al. 2008*a*, and the present paper), contrary to what would be expected if the surface brightness deviation was indeed due solely to excess H-band emission from a young stellar population. This is illustrated in Figure 9*f*. In this panel and all others of Figure 9, ULIRGs are open symbols and PG QSOs are filled symbols.

The other panels of Figure 9 confirm the clear trend with half-light radii (*a*, the probability that this correlation is fortuitous is  $P[null] = 0.02\%$ ) and reveal a possible tendency for PG QSOs with large infrared excesses to have brighter hosts than inactive spheroids (*b*). But there is no obvious correlation between surface brightness deviation and merger phase [as determined by the PSF-masked residuals (*c*) and the PSF-host flux ratios (*d*)] or the AGN fractional contribution to the bolometric luminosity (*e*) derived from the *Spitzer* data of Veilleux et al. (2009)<sup>5</sup>. As mentioned above, ULIRGs and PG QSOs show no displacement in the FP from each other. These results seem inconsistent at first with the idea that the surface brightness deviations in small hosts are caused solely by excess H-band emission from star formation. If ULIRGs are the precursors of PG QSOs (the *Spitzer* data of Veilleux et al. 2009 are indeed largely consistent with this scenario), the ULIRGs should have more star formation and therefore we naively expect that ULIRG hosts should deviate more from the FP of inactive spheroids than PG QSO hosts. However, as pointed out in the last paragraph of Section 4.5., removal of the nuclear starbursts in these objects during the PSF subtraction may be wiping out the expected surface brightness shift between ULIRGs and PG QSOs in

---

<sup>5</sup> These AGN contributions are calculated using six independent mid-infrared AGN indicators that give consistent results. The bolometric luminosities of ULIRGs are assumed to be  $1.15 \times L(\text{IR})$ , while the bolometric luminosities of PG QSOs are assumed to be  $7 \times L(5100 \text{ \AA}) + L(\text{IR})$  (Netzer et al. 2007). See Table 1 for a list of the bolometric luminosities.

the FP. Moreover, dust may be affecting the observed surface brightnesses and colors, particularly in ULIRG hosts, which are systematically redder than PG QSO hosts (Figure 9*f*; see also Scoville et al. 2000).

A closer examination of Figure 8*a* seems to indicate that the hosts of the more radio/X-ray luminous QSOs from Dunlop et al. (2003) are systematically *fainter* than inactive spheroids of the same size and fit rather well the extension to larger radii of the linear fit through the NICMOS data on ULIRGs and PG QSOs. If real, this result cannot be explained by excess H-band emission from star formation. However, a number of assumptions are made when plotting the data points of Dunlop et al. on Figure 8*a*. Following Paper I, we used the half-light radii measured from the R-band data of Dunlop et al. directly, without applying any color corrections, while the R-band surface brightness measurements of Dunlop et al. were shifted assuming  $R-H = 2.8$ , typical of  $M_R \approx -23.5$  elliptical systems at  $z \sim 0.2$  (Lilly & Longair 1984; Fukugita et al. 1995; Fioc & Rocca-Volmerange 1999; Hyvönen et al. 2007, 2008). Note that a smaller  $R-H$ , more in line with the average value found for the lower luminosity PG QSO hosts (Section 4.5 and Figure 7), would bring the data points of Dunlop et al. further down in Figure 8 i.e., systematically fainter than the corresponding spheroids. Positive  $R-H$  radial gradients within the hosts would increase the H-band half-light radii, but the shift between the Dunlop et al. QSOs and the inactive spheroids is too large to be explained solely by this effect. Moreover, inactive elliptical galaxies are usually redder near the center than on the outskirts so the color gradients are usually negative rather than positive (e.g., Peletier et al. 1990). The results from our comparisons of the QSO spheroid sizes at V, R, and H (Section 4.5) suggest a similar negative color gradient in QSO hosts.

Another source of uncertainty in this discussion is the exact location of the FP at half-light radii larger than 10 kpc. The catalogs of Bernardi et al. (2003) and especially Pahre (1999) contain relatively few objects of this size so the FP is not well determined from these data. Also, we assumed a color correction from  $z$ -band to H-band for the Bernardi et al. surface brightness measurements that was independent of galaxy size (and environment); this is probably an oversimplification (e.g., Figure 5 of Hyvönen et al. 2007 suggests redder colors for the more luminous hosts; see also Bernardi et al. 2006 for a discussion of a dependence on environment). Recent compilations of FP parameters among luminous inactive and active spheroids by Bernardi et al. (2006), Hamilton et al. (2008), and Wolf & Sheinis (2008) do not show any significant systematic shift between the  $r$ -band properties of active and inactive spheroids. In fact, the Hamilton et al. and Wolf & Sheinis data appear to be consistent with the FP shown in Figure 8, assuming  $V-H = 3.5$  and  $r-H = 3.0$ , respectively. So one should be cautious in attaching too much importance to the apparent shift between the Dunlop et al. data and the FP data of Figure 8*a*.



Nevertheless, the shift to *brighter* magnitudes among the small ULIRG/QSO hosts *is* definitely real. The fact that this shift does not correlate strongly with star formation/dust reddening, merger phase, and AGN strength indicators seems to indicate that it is not solely due to excess H-band emission from star formation. Figure 9*d* and 9*e* also seem to rule out the possibility that systematic residuals associated with the PSF fitting and removal procedure are causing these surface brightness deviations. At this stage, we cannot rule out the possibility that a combination of possibly severe and counteracting effects of population age, dust extinction and geometry, and residual scattered emission by the central AGN/starburst is causing this systematic shift. However, we favor a more conservative scenario where all of these effects are relatively modest. If the bulk of the emission from merger-induced star formation is nuclear, as it is known to be the case for most if not all ULIRGs and possibly also in some PG QSOs, then the host colors and excess H-band emission need not be correlated with the merger phase since the bulk of this emission was removed in the PSF subtraction procedure.

## 5.2. Black Hole Masses and Accretion Rates

The host magnitudes derived from our data can in principle be used to derive the black hole masses in the cores of these objects, assuming the relation between black hole mass and the mass of the spheroidal component in normal inactive galaxy (e.g., Magorrian et al. 1998; Kormendy & Gebhardt 2001; Marconi & Hunt 2003; Häring & Rix 2004) also applies to recent mergers. Following Paper I, we use the H-band elliptical host magnitude – black hole mass relation in Marconi & Hunt (2003),  $\log(M_{BH}) = -2.80 - (0.464 \times M_H)$ , and deduce photometrically derived black hole masses ranging from  $\sim 5 \times 10^7$  (PG 0844+349) to  $200 \times 10^7 M_\odot$  (B2 2201+31A) (Table 6). The average (median) black hole mass is  $M_{BH} = 4.4 \pm 1.0 \times 10^8 M_\odot$  ( $2.5 \times 10^8 M_\odot$ ; Table 7). This derivation neglects dust extinction outside the nuclear regions of the hosts (which would cause an underestimate of  $M_{BH}$ ) and the presence of recent or on-going non-nuclear star formation (which would have the opposite effect).

Also listed in Table 6 are the photometric black hole mass estimates for the 1-Jy ULIRGs from Paper I and Veilleux et al. (2002), and the black hole mass estimates for these ULIRGs and PG QSOs derived from three other methods, when available. The dynamical estimates are from Dasyra et al. (2006a, 2006b, 2007). They are based on stellar velocity dispersions,  $\sigma_*$ , measured from VLT/Keck near-infrared spectra and the  $M_{BH} - \sigma_*$  relation of Tremaine et al. (2002). Next, we list the black hole mass estimates for the 13 PG QSOs from the detailed reverberation mapping study of Peterson et al. (2004; updated by Bentz et al. 2006; 3C 273 is the only ULIRG with a black hole mass estimate based on this method). Finally, in

the last column of these tables, we list the black hole masses of PG QSOs from Vestergaard & Peterson (2006) based on the virial method. These virial estimates are derived from the widths of the single-epoch  $H\beta$  profiles measured by Boroson & Green (1992) and an empirical relationship between broad-line region (BLR) size and  $5100 \text{ \AA}$  luminosity that is calibrated to the improved mass measurements of nearby AGNs based on emission-line reverberation mapping.

Table 6 lists the black hole mass estimates from the four different methods. Table 7 lists the averages, medians, and standard deviations from the averages of the black hole mass estimates derived from each method. Figure 10 compares the results from the various methods on an object-by-object basis using the data in Table 6. Figures 10*b* and 10*c* indicate that the photometric, reverberation, and virial black hole mass estimates generally agree with each other to within a factor of  $\sim 3$  or better. On the other hand, the dynamical black hole mass estimates in ULIRGs (PG QSOs) are systematically smaller by a factor of  $\sim 7$  ( $\sim 3$ – $4$ ) on average than the other estimates. Figures 10*a* and 10*d* suggest that the discrepancies between the dynamical measurements and the photometric and reverberation mapping measurements increase with increasing black hole masses, while Figure 10*e* shows no obvious trend with the virial black hole masses. Note in passing that the large scatter in Figure 10*a* implies that the Faber-Jackson relation does not apply to these systems.

It is beyond the scope of this paper to try to explain the origins of these discrepancies. Here we simply describe the principal sources of uncertainties for each method. The photometric method relies on the unproven assumption that the  $M_{\text{BH}} - M_{\text{spheroid}}$  relation of Marconi & Hunt (2003) applies to recent mergers. In addition, as discussed in Section 5.1, the photometric measurements from our data may be affected by a number of effects (non-nuclear star formation and dust extinction, PSF subtraction) which could therefore add uncertainties to the photometric black hole mass estimates [similar results are found when we exclude bulge + disk systems so the uncertainties in the bulge/disk decomposition (Kim et al. 2008a, 2008b) do not appear to be a major issue here]. Note, however, that if the surface brightness deviations seen in Figure 8*a* are due to a combination of these effects, then one would expect the photometric black hole mass estimates to be overestimated in the smaller hosts with the smaller black hole masses, the opposite of what is needed to explain the trends of increasing discrepancies at larger black hole masses. To further test this hypothesis we took the worst possible scenario and assumed that the surface brightness deviations inferred from Figure 8*a* were due entirely to excess H-band emission from a young stellar population and corrected the photometric black hole masses accordingly. The results are shown by the horizontal segments in Figures 10*a* – *c*. These shifts do not significantly improve the agreement with the other methods.

The dynamical black hole mass measurements are based on two important but largely unproven assumptions: the young star probed by the CO observations of Dasyra et al. trace the full velocity dispersion of the spheroid and the  $M_{\text{BH}} - \sigma_*$  relation(s) apply to recent mergers. Recent simulations (e.g., Dasyra et al. 2006b; Johansson et al. 2009) provide support for this last assumption, but it is far from being the final word given the difficulty in modeling the complex processes associated with star formation and black hole growth on sub-pc to kpc scales. The first assumption has been discussed in the context of optically-selected merger remnants, where Ca II triplet velocity dispersion measurements are found to be systematically larger than CO measurements by a factor of up to  $\sim 2$  (Rothberg & Joseph 2006; Dasyra et al. 2006b; Rothberg 2009; see also Silge & Gebhardt 2003 in elliptical galaxies). The dynamically-derived black hole masses scale with the fourth power of the velocity dispersions, so this systematic shift between optical and near-infrared measurements could conceivably explain some of the discrepancy between the dynamical measurements and the other measurements.

Finally, the reverberation mapping and virial measurements are widely considered to be the most reliable estimates of black hole masses. However, they too are subject to possibly significant uncertainties. In particular, the scale factor  $f$ , which accounts for the unknown geometry, kinematics, inclination of the broad-line region, may depend on luminosity and accretion rate (e.g., Collin et al. 2006). The value adopted by Peterson et al. (2004) and Vestergaard & Peterson (2006),  $f = 5.5$ , was derived from lower luminosity AGN (Onken et al. 2004) and may not apply to the higher luminosity PG QSOs of our sample (see Dasyra et al. 2007 and Watson et al. 2008 for a more detailed discussion of the origins of the discrepancies between the dynamical and reverberation mapping methods).

Given the substantial uncertainties affecting all of the black hole mass measurements, it is in fact remarkable that a large subset of these measurements agree with each other to within of  $\sim 3$  or better. In the following discussion, we adopt our photometric black hole mass estimates at face value, keeping in mind of the possibly large uncertainties on these black hole mass estimates, and derive the Eddington ratio i.e., the ratio of AGN bolometric luminosity to the Eddington luminosity,  $L_{\text{Edd}} = 3.3 \times 10^4 M_{\text{BH}}/M_{\odot} L_{\odot}$ , for each system. This ratio is an objective indicator of the level of nuclear activity in these systems. The AGN fractional contributions to the bolometric luminosities of the PG QSOs and ULIRGs are taken directly from our *Spitzer* study (Veilleux et al. 2009; see details in footnote #5 in Section 5.1). Some of the results have already been discussed in Veilleux et al. (2009) and are not repeated here. Figure 11 focuses exclusively on the ULIRGs and radio-quiet and radio-loud PG QSOs in the *HST* sample. These three classes of objects have statistically the same photometric Eddington ratios, of order  $\sim 3\text{-}30\%$  ( $\sim 10\%$  on average). This result is similar to those derived by McLeod & McLeod (2001). Interestingly, none of the ULIRGs

and PG QSOs in our sample require super-Eddington mass accretion rates. This remains true for all but two objects after we correct the spheroid host magnitudes for possible excess H-band emission from young stellar population (indicated by the horizontal segments in Figure 11). The corrected Eddington ratios are then  $\sim 30\%$  on average.

## 6. Conclusions

As part of QUEST, we have supplemented our original *HST* NICMOS H-band imaging data set on 7 PG QSOs from Paper I with an additional set of 21 PG QSOs, for a total of 28 objects. The results from our detailed two-dimensional analysis of this larger PG QSO sample were then compared with the data from Paper I on ULIRGs, which were analyzed exactly in the same way, and those from literature. The main conclusions of our study are the followings:

- The majority (57%) of the PG QSOs show signs of a recent galactic interaction.
- Eleven (39%) PG QSOs show a prominent elliptical morphology, nine (32%) have a distinct stellar disk in addition to a central bulge, and the others have a morphology that is ambiguous either due to severe merger-induced disturbances (5/28, 18%) or mismatch in the point-spread function (3/28, 11%).
- The fraction of QSOs with elliptical host is larger among QSOs with undetected FIR emission, small infrared excess, and luminous hosts.
- The hosts of FIR-bright QSOs show a tendency to have more pronounced merger-induced morphological anomalies and smaller QSO-to-host luminosity ratios on average than the hosts of FIR-faint QSOs.
- The host sizes and luminosities of the radio-quiet (radio-loud) PG QSOs in our sample are statistically indistinguishable from (larger than) those of the 26 highly-nucleated ULIRG hosts presented in Paper I. ULIRGs, radio-quiet PG QSOs, and radio-loud PG QSOs with elliptical hosts lie close to, but not exactly on, the FP of inactive spheroids. We confirm the tendency noted in Paper I for objects with small ( $\lesssim 2$  kpc) spheroids to be up to 1 mag. brighter than normal inactive spheroids. Comparisons of our H-band host magnitudes and sizes with similar R- and V-band data taken from the literature support the existence of a young stellar population outside the nuclear region of several PG QSOs and ULIRGs which may contribute to the observed excess H-band emission. However, no obvious trend is seen between this excess H-band emission

and host R–H color, merger phase, or AGN indicators in ULIRGs and PG QSOs, suggesting that other effects like dust extinction are also at play. PSF subtraction may also wipe out correlations with merger phase in systems with strong merger-induced nuclear starbursts (i.e., most ULIRGs and possibly some PG QSOs).

- The H-band spheroid-host luminosities of the PG QSOs, uncorrected for extinction or the presence of a young stellar population, imply black hole masses ranging from  $\sim 5$  to  $200 \times 10^7 M_{\odot}$ . These values are similar to those of the ULIRGs from Paper I, within a factor of  $\sim 3$  from black hole mass estimates based on the reverberation mapping and virial methods, but significantly larger than those derived from the stellar velocity dispersion method. These discrepancies are arguably within the range of the large uncertainties on all these measurements.
- Sub-Eddington mass accretion rates of order  $\sim 3\text{--}30\%$  are implied for all PG QSOs and ULIRGs in our sample when the photometric black hole mass estimates are combined with our published *Spitzer* estimates of the AGN contributions to the bolometric luminosities in these objects. Corrections due to possible excess H-band emission from a young circumnuclear stellar population increase the average mass accretion rate by a factor of  $\sim 3$ .

By and large, these results and those of Paper I support the merger scenario where QSO activity of moderate luminosity is triggered by major galaxy mergers that result in the formation of intermediate-mass spheroids. The weaker merger-induced morphological anomalies found among Seyfert-like ULIRGs (Paper I) and PG QSOs with elliptical hosts and small infrared excess indicate that nuclear activity is indeed seen preferentially in late-stage mergers. The disk components, detected in all QSOs with AGN bolometric luminosities less than  $\sim 10^{11.5} L_{\odot}$ , can be explained in this merger scenario if substantial and rapid accretion of residual gas took place after the merger.

S.V., D.C.K., and D.S.N.R. were supported in part by NASA through grant HST-GO-10906.01-A. S. V. acknowledges support from a Senior Award from the Alexander von Humboldt Foundation and thanks the host institution, MPE Garching, where some of this work was performed. C.Y.P. is grateful to Space Telescope Science Institute for support through the Institute Fellowship program and to the National Research Council of Canada through the Plaskett Fellowship program at the Herzberg Institute of Astrophysics. We thank R. Davies, K. Jahnke, and E. Bell for comments on an earlier version of the manuscript, and the anonymous referee for a thoughtful review. This work has made use of NASA’s Astrophysics Data System Abstract Service and the NASA/IPAC Extragalactic Database (NED),

which is operated by the Jet Propulsion Laboratory, California Institute of Technology, under contract with the National Aeronautics and Space Administration.

## REFERENCES

- Bentz, M. C., et al. 2006, *ApJ*, 651, 775
- Bergeron, L. E., & Dickinson, M. E. 2003, Instrument Science Report NICMOS 2003-010
- Best, P. N., et al. 2007, *MNRAS*, 379, 894
- Canalizo, G., Stockton, A., Brotherton, M. S., & Lacy, M. 2006, *NewA Rev.*, 50, 650
- Canalizo, G., et al. 2007, *ApJ*, 669, 801
- Choi, Y., Goto, T., & Yoon, S.-J. 2009, preprint (astro-ph/0904.1209)
- Collin, S., Kawaguchi, T., Peterson, B. M., & Vestergaard, M. 2006, *A&A*, 456, 75
- Dasyra, K. M., et al. 2006a, *ApJ*, 638, 745
- Dasyra, K. M., et al. 2006b, *ApJ*, 651, 835
- Dasyra, K. M., et al. 2007, *ApJ*, 657, 102
- Dickinson, M. E., et al. 2002, in *HST NICMOS Data Handbook v. 5.0*, ed. B. Mobasher, Baltimore, STScI
- Dunlop, J. S., McLure, R. J., Kukula, M. J., Baum, S. A., O’Dea, C. P., & Hughes, D. H. 2003, *MNRAS*, 340, 1095
- Fioc, M., & Rocca-Volmerange, B. 1999, *A&A*, 351, 869
- Fukugita, M., Shimasaku, K., & Ichikawa, T. 1995, *PASP*, 107, 945
- Gonzaga, S., Biretta, J. A., Wiggs, M. S., Hsu, J. C., Smith, T. E., Bergeron, L., and the WFPC2 Group, 1998, Instrument Science Report WFPC2 98-04.
- Governato, F., et al. 2008, *MNRAS*, preprint (astro-ph/0812.0379)
- Graves, G. J., Faber, S. M., & Schiavon, R. P. 2009, preprint (astro-ph/0903.3603)
- Guyon, O., Sanders, D. B., & Stockton, A. 2006, *ApJS*, 166, 89
- Hamilton, T. S., Casertano, S., & Turnshek, D. A. 2008, *ApJ*, 678, 22
- Häring, N., & Rix, H.-W. 2004, *ApJ*, 604, L89
- Hopkins, P. F., et al. 2009, *ApJ*, 691, 1424
- Hyvönen, T., et al. 2007, *A&A*, 476, 723
- Hyvönen, T., et al. 2008, *RMxAC*, 32, 161
- Jahnke, K., Kuhlbrodt, B., & Wisotzki, L. 2004, *MNRAS*, 352, 399
- Jahnke, K., Wisotzki, L., Courbin, F., & Letawe, G. 2007, *MNRAS*, 378, 23
- Johansson, P. H., Naab, T., & Burkert, A. 2009, *ApJ*, 690, 802

- Kim, M., et al. 2008a, *ApJ*, 687, 767
- Kim, M., et al. 2008b, *ApJS*, 179, 283
- Kormendy, J., & Gebhardt, K. 2001, Texas Symposium on relativistic astrophysics, 20th, held in Austin, Texas, Ed JC Wheeler and H Martel, New York, American Institute of Physics, Vol. 586, 363
- Lilly, S. J., & Longair, M. S. 1984, *MNRAS*, 211, 833
- Magorrian, J., et al. 1998, *AJ*, 115, 2285
- Marconi, A., & Hunt, L. K. 2003, *ApJ*, 589, L21
- McLeod, K. K., & McLeod, B. A. 2001, *ApJ*, 546, 782
- Miller, J. S., & Sheinis, A. I. 2003, *ApJ*, 588, L9
- Netzer, H., et al. 2007, *ApJ*, 666, 806
- Onken, C. A., et al. 2004, *ApJ*, 615, 645
- Pahre, M. A. 1999, *ApJS*, 124, 127
- Peletier, R., Valentijn, E., & Jameson, R. 1990, *A&A*, 233, 62
- Peng, C., Ho, L. C., Impey, C. D., & Rix, H.-W. 2002, *AJ*, 124, 266
- Peterson, B. M., et al. 2004, *ApJ*, 613, 682
- Rothberg, B. 2009, preprint (astro-ph/0902.1725)
- Rothberg, B., & Joseph, R. D. 2006, *AJ*, 131, 185
- Sanders, D. B., et al. 1988, *ApJ*, 325, 74
- Schmidt, M., & Green, R. F. 1983, *ApJ*, 269, 352
- Schweitzer, M., et al. 2006, *ApJ*, 649, 79
- Schweitzer, M., et al. 2008, *ApJ*, 679, 101
- Scoville, N. Z., et al. 2000, *AJ*, 119, 991
- Silge, J. D., & Gebhardt, K. 2003, *AJ*, 125, 2809
- Soifer, B. T., et al. 2000, *AJ*, 119, 509
- Storchi-Bergmann, et al. 2007, *ApJ*, 670, 959
- Surace, J. A., Sanders, D. B., & Evans, A. S. 2001, *AJ*, 122, 2791
- Tremaine, S., et al. 2002, *ApJ*, 574, 740
- Veilleux, S., Kim, D.-C., & Sanders, D. B. 2002, *ApJS*, 143, 315
- Veilleux, S., Sanders, D. B., & Kim, D.-C. 1997, *ApJ*, 484, 92



- Veilleux, S., Sanders, D. B., & Kim, D.-C. 1999, *ApJ*, 522, 139
- Veilleux, S., et al. 2006, *ApJ*, 643, 707 (Paper I)
- Veilleux, S., et al. 2009, *ApJS*, June issue, in press (astro-ph/0905.1577)
- Watson, L. C., et al. 2008, *ApJ*, 682, L21
- Wolf, M. J., & Sheinis, A. I. 2008, *AJ*, 136, 1587
- Zibetti, S., et al. 2002, *ApJ*, 579, 261

Table 1. Sample

Name (1)	Other Name (2)	$z$ (3)	$\log\left(\frac{L_B}{L_\odot}\right)$ (4)	$\log\left(\frac{L_{IR}}{L_\odot}\right)$ (5)	$\log\left(\frac{L_{BOL}}{L_\odot}\right)$ (6)	$\frac{L_{IR}}{L_B}$ (7)	$\frac{L_{IR}}{L_{BOL}}$ (8)	$\frac{f_{25}}{f_{60}}$ (9)	Radio (10)	FIR Class (11)
PG0007+106	III Zw 2	0.089	-22.28	11.44	12.23	24.6	0.16	0.765	L	Weak
PG0026+129	...	0.142	-23.84	<11.47	12.07	<3.31	<0.25	<0.410	Q	Undetected
PG0050+124	I Zw 1	0.061	-22.68	11.87	12.07	29.5	0.63	0.382	Q	Strong
PG0157+001	Mrk 1014	0.163	-24.57	12.63	12.69	44.7	0.87	0.243	Q	Strong
PG0838+770	VII Zw 244	0.131	-21.55	11.45	11.76	12.9	0.49	0.455	Q	Weak
PG0844+349	...	0.064	-22.19	10.93	11.44	2.14	0.31	0.628	Q	Weak
PG0923+201	...	0.190	-24.23	<12.12	12.45	<20.9	<0.47	<0.322	Q	Undetected
PG1001+054	...	0.161	-22.94	11.56	11.86	9.12	0.50	0.456	Q	Strong
PG1116+215	...	0.176	-24.48	<11.95	12.54	<7.59	<0.26	<0.486	Q	Undetected
PG1119+120	Mrk 734	0.050	-21.65	11.08	11.33	9.12	0.56	0.501	Q	Weak
PG1126-041	Mrk 1298	0.060	-22.23	11.29	11.52	21.4	0.59	0.329	Q	Strong
PG1229+204	Mrk 771	0.063	-21.76	11.03	11.56	5.13	0.30	0.637	Q	Weak
PG1302-102	...	0.278	-25.68	12.41	12.74	7.24	0.47	0.351	L	Strong
PG1307+085	...	0.155	-23.75	...	12.34	...	...	0.412	Q	Weak
PG1309+355	...	0.184	-24.26	<11.87	12.31	<7.41	<0.36	<0.681	L	Undetected
PG1411+442	...	0.090	-23.07	11.32	11.78	6.46	0.35	0.841	Q	Weak
PG1426+015	Mrk 1383	0.086	-22.27	11.47	11.92	10.5	0.35	0.585	Q	Weak
PG1435-067	...	0.126	-23.32	<11.53	11.91	<8.51	<0.42	0.200	Q	Strong
PG1440+356	Mrk 478	0.079	-22.62	11.48	11.80	12.3	0.48	0.303	Q	Strong
PG1613+658	Mrk 876	0.129	-24.01	11.97	12.29	19.1	0.48	0.330	Q	Strong
PG1617+175	Mrk 877	0.112	-23.08	<11.25	11.74	<5.62	<0.32	<0.526	Q	Undetected
PG1626+554	...	0.133	-23.28	<11.19	11.83	<6.17	<0.23	0.063:	Q	?
PG1700+518	...	0.292	-25.49	12.59	13.12	13.5	0.30	0.474	Q	Weak
PG2130+099	Mrk 1513	0.063	-22.56	11.35	11.77	10.5	0.38	0.639	Q	Weak
B2 2201+31A	4C +31.63	0.295	-25.33	<12.52	13.27	...	<0.18	<0.279	L	Undetected
PG2214+139	Mrk 304	0.066	-22.31	<11.08	11.77	<7.08	<0.20	0.260	Q	?
PG2251+113	4C +11.72	0.326	-25.17	<12.15	12.97	<8.13	<0.15	<0.772	L	Undetected
PG2349-014	4C -01.61	0.174	-24.17	11.89	12.58	...	0.20	0.413	L	Strong

Col 1: Object name.

Col 2: Other name.

Col 3: Redshift.

Col 4: Blue luminosity.

Col 5: Infrared luminosity calculated from prescription of Sanders & Mirabel (1996).

Col 6: Bolometric luminosity calculated from  $7 \times L(5100\text{\AA}) + L(\text{IR})$  (Netzer et al. 2007).

Col 7: Ratio of infrared to blue luminosities.

Col 8: Ratio of infrared to bolometric luminosities.

Col 9:  $f_{25}/f_{60}$  flux ratio. Object with colon is uncertain.

Col 10: Radio loudness (Q: radio quiet, L: radio loud) from Kellermann et al (1994) except for two objects (B2 2201+31A and PG2349-014 from Becker et al., 1991).

Col 11: FIR strength according to Netzer et al. (2007).

Table 2. One Galaxy Component Fits

Name (1)	n (2)	$r_{1/2}$ (3)	b/a (4)	PA (5)	$m_n$ (6)	$M_n$ (7)	$m_{PSF}$ (8)	$M_{PSF}$ (9)	$R_1$ (10)	$R_2$ (11)	$\chi^2_{\nu 1}$ (12)	$\chi^2_{\nu 2}$ (13)
PG0007+106	1.0	1.79	0.93	134.4	14.47	-23.59	13.58	-24.48	64.2	45.7	8.6	1.5
	4.0	2.97	0.92	137.9	13.88	-24.18	13.63	-24.43	36.9	22.9	6.2	0.5
	7.2	5.33	0.92	137.4	13.53	-24.53	13.67	-24.39	35.2	22.0	6.0	0.5
PG0026+129	1.0	2.07	0.85	-64.9	15.74	-23.40	13.40	-25.74	92.9	9.3	27.6	1.3
	4.0	0.90	0.83	111.6	15.14	-24.00	13.47	-25.67	69.8	7.0	26.4	1.3
	5.5	0.95	0.80	110.3	15.16	-23.98	13.46	-25.68	71.1	6.9	26.3	1.3
PG0050+124 <sup>(a)</sup>	1.0	2.38	0.82	30.6	12.77	-24.42	12.12	-25.07	55.7	15.1	234.3	86.7
	4.0	1.64	0.83	35.2	12.36	-24.83	12.25	-24.94	37.5	10.5	163.9	68.6
	2.9	1.79	0.83	34.3	12.45	-24.74	12.21	-24.98	38.8	10.5	158.9	62.2
PG0157+001	1.0	1.06	0.92	-23.5	14.32	-25.15	13.86	-25.61	62.6	46.2	14.7	6.3
	4.0	1.82	0.92	-37.4	13.82	-25.65	13.86	-25.61	39.5	27.3	7.1	1.7
	13.0	3.47	0.90	-38.1	13.25	-26.22	14.07	-25.40	30.7	20.7	6.3	1.1
PG0838+770 <sup>(a)</sup>	1.0	5.95	0.42	83.1	14.33	-24.62	14.88	-24.07	36.0	25.6	7.1	2.0
	4.0	10.67	0.52	83.4	13.75	-25.20	14.98	-23.97	25.4	17.2	5.5	2.0
	3.7	9.90	0.52	83.4	13.80	-25.15	14.97	-23.98	25.5	17.1	5.5	1.9
PG0844+349	1.0	1.72	0.73	117.8	13.99	-23.30	13.00	-24.29	51.3	18.0	27.9	2.0
	4.0	2.38	0.76	119.5	13.48	-23.81	13.06	-24.23	39.6	11.4	24.8	1.4
	3.9	2.36	0.76	119.5	13.50	-23.79	13.06	-24.23	39.6	11.4	25.4	1.4
PG0923+201	1.0	1.90	0.96	67.4	15.50	-24.33	13.69	-26.14	95.6	19.8	12.2	1.7
	4.0	1.30	0.96	61.6	14.95	-24.88	13.78	-26.05	56.0	7.7	10.2	1.2
	9.6	1.01	0.95	61.2	14.57	-25.26	13.87	-25.96	41.1	4.3	9.8	1.2
PG1001+054	1.0	2.33	0.50	159.5	16.22	-23.21	14.27	-25.16	63.3	15.3	3.6	1.1
	4.0	2.38	0.53	159.4	15.76	-23.67	14.31	-25.12	52.1	11.6	3.5	1.1
	2.1	2.30	0.52	159.5	15.99	-23.44	14.29	-25.14	55.8	12.3	3.5	1.1
PG1116+215	1.0	5.17	0.73	71.9	15.30	-24.36	12.50	-27.16	281.0	14.6	31.6	1.1
	4.0	7.02	0.71	70.9	14.91	-24.75	12.51	-27.15	258.5	13.7	32.3	1.4
	1.7	5.44	0.74	71.6	15.13	-24.53	12.51	-27.15	260.5	12.1	31.8	1.1
PG1119+120	1.0	0.85	0.97	-140.5	13.52	-23.23	13.23	-23.52	47.1	30.8	21.4	19.6
	4.0	1.20	0.96	-163.8	12.99	-23.76	13.34	-23.41	28.4	17.4	12.3	10.8
	3.4	1.12	0.96	-162.6	13.06	-23.69	13.32	-23.43	28.3	16.9	12.2	11.0
PG1126-041	1.0	2.38	0.40	153.8	13.42	-23.73	12.33	-24.82	63.5	30.4	52.6	4.7
	4.0	4.52	0.42	152.5	12.79	-24.36	12.36	-24.79	46.1	16.3	49.0	2.9
	3.5	4.06	0.42	152.6	12.86	-24.29	12.36	-24.79	45.7	15.9	49.0	2.8
PG1229+204 <sup>(a)</sup>	1.0	4.33	0.64	28.8	13.14	-24.12	13.56	-23.70	37.1	20.4	110.8	69.5
	4.0	4.33	0.73	29.2	12.72	-24.54	13.72	-23.54	20.2	15.5	60.0	57.0
	3.4	4.13	0.73	29.1	12.78	-24.48	13.70	-23.56	20.7	15.7	59.3	55.8
PG1302-102	1.0	6.69	0.68	140.3	15.70	-25.07	14.11	-26.66	72.8	13.1	10.0	3.5
	4.0	10.33	0.69	136.6	15.21	-25.56	14.13	-26.64	70.7	14.9	10.0	3.9
	1.7	7.28	0.68	139.4	15.55	-25.22	14.11	-26.66	73.5	13.7	10.0	3.6
PG1307+085	1.0	1.67	0.95	85.5	15.71	-23.64	14.06	-25.29	52.6	14.2	4.6	1.3
	4.0	1.32	0.94	98.2	15.21	-24.14	14.13	-25.22	30.7	5.3	3.6	1.1
	5.8	1.21	0.94	100.8	15.06	-24.29	14.17	-25.18	27.5	4.9	3.6	1.1
PG1309+355	1.0	3.15	0.86	5.1	14.80	-24.96	13.94	-25.82	44.5	8.8	23.7	1.7
	4.0	3.49	0.87	4.4	14.32	-25.44	14.02	-25.74	31.6	3.1	17.8	0.9
	4.4	3.09	0.88	4.1	14.36	-25.40	14.03	-25.73	32.1	4.3	17.8	1.1

Table 2—Continued

Name (1)	n (2)	$r_{1/2}$ (3)	b/a (4)	PA (5)	$m_n$ (6)	$M_n$ (7)	$m_{PSF}$ (8)	$M_{PSF}$ (9)	$R_1$ (10)	$R_2$ (11)	$\chi^2_{\nu 1}$ (12)	$\chi^2_{\nu 2}$ (13)
PG1411+442	1.0	1.25	0.89	42.6	14.54	−23.52	12.86	−25.20	78.4	27.9	33.3	6.0
	4.0	1.37	0.90	22.3	14.00	−24.06	12.91	−25.15	58.4	16.7	29.4	4.0
	14.9	2.64	0.89	−163.7	13.37	−24.69	13.00	−25.06	47.6	13.7	28.9	3.8
PG1426+015 <sup>(a)</sup>	1.0	2.04	0.92	85.3	13.78	−24.20	13.08	−24.90	46.8	25.0	21.4	14.7
	4.0	3.62	0.92	81.6	13.19	−24.79	13.14	−24.84	32.1	14.0	18.0	12.3
	4.1	3.70	0.92	81.6	13.17	−24.81	13.14	−24.84	32.1	14.0	18.0	12.3
PG1435−067	1.0	2.48	0.89	32.5	15.95	−22.91	14.22	−24.64	59.3	20.7	4.1	1.4
	4.0	2.14	0.80	42.3	15.55	−23.31	14.27	−24.59	44.4	17.3	3.3	1.4
	5.2	1.94	0.78	43.0	14.51	−24.35	14.28	−24.58	43.1	17.8	3.2	1.5
PG1440+356	1.0	1.00	0.78	57.5	13.86	−23.92	12.53	−25.25	62.5	28.0	29.0	2.9
	4.0	1.14	0.77	58.3	13.32	−24.46	12.60	−25.18	35.1	11.1	21.8	0.8
	10.5	1.72	0.76	58.6	12.87	−24.91	12.68	−25.10	26.1	5.8	21.0	0.5
PG1613+658	1.0	3.20	0.88	−39.1	13.75	−25.16	13.11	−25.80	54.0	36.4	12.4	5.0
	4.0	6.80	0.85	−33.1	13.09	−25.82	13.15	−25.76	33.9	20.1	9.9	4.0
	9.0	13.82	0.82	−35.0	12.77	−26.14	13.20	−25.71	34.8	21.6	9.4	4.5
PG1617+175	1.0	2.62	0.79	−9.2	15.40	−23.19	13.34	−25.25	83.7	8.1	11.3	1.0
	4.0	2.60	0.79	−2.0	14.95	−23.64	13.37	−25.22	70.6	10.0	11.0	1.2
	2.9	2.46	0.79	−4.0	15.06	−23.53	13.37	−25.22	70.8	9.2	11.0	1.1
PG1626+554	1.0	3.90	0.96	−64.1	15.15	−23.83	13.80	−25.18	53.9	22.0	7.2	1.0
	4.0	5.53	0.95	−55.9	14.67	−24.31	13.84	−25.14	39.0	14.8	6.2	0.9
	11.8	18.18	0.95	−48.7	14.02	−24.96	13.88	−25.10	36.0	14.9	6.1	1.1
PG1700+518	1.0	4.46	0.90	−156.9	15.94	−24.95	13.16	−27.73	138.7	30.9	18.5	5.4
	4.0	2.54	0.90	−149.9	15.48	−25.41	13.19	−27.70	106.9	24.9	17.9	5.7
	7.8	1.75	0.90	−147.5	15.21	−25.68	13.22	−27.67	89.2	21.2	17.7	5.9
PG2130+099	1.0	5.17	0.54	−132.2	13.46	−23.80	12.33	−24.93	56.7	26.6	125.0	89.0
	4.0	6.04	0.55	−129.8	12.93	−24.33	12.39	−24.87	33.9	17.8	70.9	58.6
	8.3	11.02	0.54	−128.9	12.54	−24.72	12.42	−24.84	31.1	16.1	67.8	55.8
B2 2201+31A	1.0	6.52	0.58	−52.2	15.10	−25.82	13.69	−27.23	46.9	19.2	5.1	1.3
	4.0	9.91	0.58	−53.2	14.56	−26.36	13.72	−27.20	31.3	8.4	4.2	0.9
	3.6	9.30	0.58	−53.1	14.62	−26.30	13.72	−27.20	31.6	8.6	4.2	0.9
PG2214+139 <sup>(a)</sup>	1.0	1.62	0.96	64.9	13.33	−24.03	12.96	−24.40	37.0	20.7	17.4	2.1
	4.0	2.78	0.95	64.0	12.75	−24.61	13.02	−24.34	17.4	6.1	11.0	0.4
	4.8	2.69	0.95	64.1	12.77	−24.59	13.04	−24.32	20.6	9.1	10.8	0.6
PG2251+113	1.0	8.99	0.71	78.2	16.53	−24.63	13.57	−27.59	242.3	18.0	16.1	1.0
	4.0	21.52	0.63	75.6	15.94	−25.22	13.58	−27.59	238.8	21.8	16.3	1.0
	0.7	9.65	0.71	77.8	16.47	−24.69	13.57	−27.59	255.0	19.5	16.0	1.0
PG2349−014	1.0	4.58	0.76	96.7	14.44	−25.18	13.38	−26.24	47.3	24.8	12.4	1.3
	4.0	8.13	0.75	99.2	13.84	−25.78	13.42	−26.20	33.5	14.5	10.4	0.7
	8.0	7.36	0.75	97.2	13.85	−25.77	13.46	−26.16	38.1	19.6	10.0	1.1

Col 1: Object name.

Col 2: Sérsic index.

Col 3: Half-light radius in kpc of Sérsic component.

Col 4: Axis ratio of Sérsic component.

Col 5: Position angle (East of North) of major axis of Sérsic component.

*Col 6:* Apparent H magnitude of Sérsic component.

*Col 7:* Absolute H magnitude of Sérsic component.

*Col 8:* Apparent H magnitude of PSF component.

*Col 9:* Absolute H magnitude of PSF component.

*Col 10:* Absolute residuals normalized to total host galaxy flux (%). See Section 4.3 for more detail.

*Col 11:* PSF-masked absolute residuals normalized to total host galaxy flux (%). The central PSF region brighter than 11 H mag arcsec<sup>-2</sup> was masked for these calculations. See Section 4.3 for more detail.

*Col 12:* Reduced  $\chi^2$  value.

*Col 13:* PSF-masked reduced  $\chi^2$  value. The central PSF region brighter than 11 H mag arcsec<sup>-2</sup> was masked for these calculations.

<sup>(a)</sup> Entries for this object are uncertain because the host galaxy fills most of the field of view so the sky background is not well determined.

Table 3. Two Galaxy Components Fits

Name	n	$r_{\frac{1}{2}}$	b/a	PA	$m_n$	$M_n$	$m_{PSF}$	$M_{PSF}$	$R_1$	$R_2$	$\chi^2_{\nu 1}$	$\chi^2_{\nu 2}$
(1)	(2)	(3)	(4)	(5)	(6)	(7)	(8)	(9)	(10)	(11)	(12)	(13)
PG0007+106	1.0	5.28	0.84	148.2	14.67	−23.39	13.67	−24.39	33.6	20.5	6.0	0.4
	4.0	0.93	0.93	127.2	14.61	−23.45						
PG0026+129	1.0	4.92	0.85	77.6	15.98	−23.16	13.47	−25.67	65.5	4.1	25.7	1.2
	4.0	0.35	0.80	−65.0	15.46	−23.68						
PG0050+124 <sup>(a)</sup>	1.0	3.35	0.88	37.5	13.76	−23.43	12.26	−24.93	36.4	9.9	154.5	59.8
	4.0	1.03	0.79	34.5	12.76	−24.43						
PG0157+001	1.0	9.92	0.89	−6.6	14.59	−24.88	13.95	−25.52	31.5	20.8	6.0	1.1
	4.0	0.90	0.90	−37.4	14.05	−25.42						
PG0838+770 <sup>(a)</sup>	1.0	8.82	0.35	82.4	14.36	−24.59	15.15	−23.80	22.9	16.3	4.1	1.3
	4.0	0.56	0.93	143.0	15.55	−23.40						
PG0844+349	1.0	2.78	0.68	125.7	14.11	−23.18	13.12	−24.17	35.2	10.0	24.0	1.1
	4.0	0.28	0.79	104.0	14.60	−22.69						
PG1001+054	1.0	2.85	0.30	162.3	16.96	−22.47	14.30	−25.13	52.4	11.3	3.4	1.1
	4.0	1.66	0.83	130.9	16.45	−22.98						
PG1119+120	1.0	2.35	0.64	160.3	13.99	−22.76	13.41	−23.34	22.9	11.9	12.4	9.2
	4.0	0.45	0.84	−120.1	13.63	−23.12						
PG1126−041	1.0	4.14	0.33	146.0	13.60	−23.55	12.36	−24.79	49.2	17.7	49.9	2.8
	4.0	0.79	0.65	147.0	14.16	−22.99						
PG1229+204 <sup>(a)</sup>	1.0	5.35	0.31	30.4	14.53	−22.73	13.70	−23.56	18.7	14.2	51.1	48.2
	4.0	3.65	0.96	13.9	13.02	−24.24						
PG1426+015 <sup>(a)</sup>	1.0	6.59	0.46	49.4	14.18	−23.80	13.15	−24.83	27.2	9.9	17.1	11.8
	4.0	1.64	0.79	125.4	13.91	−24.07						
PG1440+356	1.0	4.19	0.58	49.8	14.19	−23.59	12.66	−25.12	28.6	8.3	20.5	0.5
	4.0	0.39	0.81	64.4	13.64	−24.14						
PG1626+554	1.0	4.73	0.96	−71.4	15.11	−23.87	15.26	−23.72	13.2	5.8	4.9	0.9
	4.0	0.05	0.61	−170.0	14.06	−24.92						
PG2130+099	1.0	16.29	0.54	−111.4	13.98	−23.28	12.40	−24.86	31.8	16.3	64.8	46.4
	4.0	2.83	0.55	−133.5	13.34	−23.92						

Col 1: Object name.

Col 2: Sérsic index.

Col 3: Half-light radius in kpc of Sérsic component.

Col 4: Axis ratio of Sérsic component.

Col 5: Position angle (East of North) of major axis of Sérsic component.

Col 6: Apparent H magnitude of Sérsic component.

Col 7: Absolute H magnitude of Sérsic component.

Col 8: Apparent H magnitude of PSF component.

Col 9: Absolute H magnitude of PSF component.

Col 10: Absolute residuals normalized to total host galaxy flux (%). See Section 4.3 for more detail.

Col 11: PSF-masked absolute residuals normalized to total host galaxy flux (%). The central PSF region brighter than 11 H mag arcsec<sup>−2</sup> was masked for these calculations. See Section 4.3 for more detail.

Col 12: Reduced  $\chi^2$  value.

*Col 13*: PSF-masked reduced  $\chi^2$  value. The central PSF region brighter than 11 H mag arcsec<sup>-2</sup> was masked for these calculations.

<sup>(a)</sup> Entries for this object are uncertain because the host galaxy fills most of the field of view so the sky background is not well determined.

Table 4. Details of PG QSO Small Structure

Name	$\Delta$ R.A.	$\Delta$ Dec.	$r_{\frac{1}{2}}$	$m_H$
(1)	(2)	(3)	(4)	(5)
PG1119+120	-0.6	2.8	0.87	16.00
PG1302–102 #1	-0.6	0.9	0.51	16.96
PG1302–102 #2	0.0	2.4	0.84	17.91
PG1411+442	-1.2	-1.8	0.57	16.81
PG1426+015	1.3	-2.1	0.41	15.93
PG1613+658	-2.2	0.8	0.76	15.52
PG2349–014	1.9	-0.4	1.13	18.55

*Col 1:* Object name.

*Col 2 - Col 3:* Offsets relative to the QSO nucleus.

*Col 4:* Half-light radius in kpc of Sérsic component.

*Col 5:* Apparent H magnitude of component.



Table 5. Summary<sup>(a)</sup>

Name	$M_{total}$	$M_{PSF}$	$M_{host}$	$M_{model}$	$\frac{I_{PSF}}{I_{host}}$	$\frac{I_{model}}{I_{host}}$	$r_{\frac{1}{2}}$	$\langle \mu_{\frac{1}{2}} \rangle$	Visual Features			MC	IC
									Bar	Arms	Dis.		
(1)	(2)	(3)	(4)	(5)	(6)	(7)	(8)	(9)	(10)	(11)	(12)	(13)	(14)
PG0007+106	-25.03	-24.43	-24.11	-24.18	1.34	1.07	2.97	17.13	No	Yes	Yes	E	IVb
PG0026+129	-25.92	-25.67	-24.21	-24.00	3.84	0.82	0.90	14.92	No	No	Yes	E	V
PG0050+124 <sup>(b)</sup>	-25.62	-24.93	-24.81	-24.79	1.12	0.99	1.03	14.45	No	Yes	Str	B+D	IVb
PG0157+001	-26.48	-25.61	-25.84	-25.65	0.80	0.83	1.82	14.88	No	Yes	Str	E	IVb
PG0838+770 <sup>(b)</sup>	-25.21	-23.80	-24.87	-24.90	0.37	1.03	0.56	14.45	Yes	Yes	Yes	B+D	IVb
PG0844+349	-24.73	-24.17	-23.74	-23.72	1.50	0.98	0.28	13.40	No	Yes	Yes	B+D	IVb
PG0923+201	-26.34	-26.05	-24.74	-24.88	3.34	1.14	1.30	15.01	No	No	No	E	V
PG1001+054	-25.34	-25.12	-23.49	-23.67	4.50	1.18	2.38	17.43	Yes?	Yes?	Yes?	E	V
PG1116+215	-27.21	-27.16	-23.84	-24.36	21.10	1.60	...	...	No	No	No	?	V
PG1119+120	-24.28	-23.34	-23.69	-23.70	0.72	1.02	0.45	13.94	No	No	No	B+D	V
PG1126-041	-25.27	-24.79	-24.15	-24.06	1.80	0.92	0.79	15.32	No	Yes?	Yes?	B+D	V
PG1229+204 <sup>(b)</sup>	-24.80	-23.56	-24.38	-24.48	0.47	1.10	3.65	17.41	Yes	Yes	No	B+D	V
PG1302-102	-26.89	-26.66	-25.09	-25.07	4.27	0.99	...	...	No	No	Yes?	A	V
PG1307+085	-25.52	-25.22	-23.97	-24.14	3.15	1.17	1.32	15.66	No	No	No	E	V
PG1309+355	-26.32	-25.74	-25.38	-25.44	1.39	1.06	3.49	16.58	No	No	No	E	V
PG1411+442	-25.51	-25.15	-24.13	-24.06	2.57	0.94	...	...	No	No	Str	A	IVb
PG1426+015 <sup>(b)</sup>	-25.49	-24.83	-24.64	-24.70	1.20	1.06	1.64	15.93	No	No	Str	B+D	IVb
PG1435-067	-24.87	-24.59	-23.29	-23.31	3.31	1.02	2.14	17.43	No	No	No	E	V
PG1440+356	-25.66	-25.12	-24.65	-24.65	1.54	1.00	0.39	12.71	No	No	No	B+D	V
PG1613+658	-26.47	-25.76	-25.68	-25.82	1.08	1.14	...	...	No	No	Str	A	IVb
PG1617+175	-25.40	-25.25	-23.19	-23.19	6.68	1.00	...	...	No	No	No	?	V
PG1626+554	-25.50	-25.14	-24.12	-24.31	2.58	1.20	5.53	18.51	No	No	No	E	V
PG1700+518	-27.83	-27.70	-25.49	-25.41	7.67	0.93	...	...	No	No	Yes	A	IVb
PG2130+099	-25.32	-24.87	-24.14	-24.40	1.90	1.24	2.83	17.17	No	Yes	No	B+D	IVb
B2 2201+31A	-27.53	-27.20	-26.08	-26.36	2.81	1.29	9.91	18.32	No	No	Yes	E	V
PG2214+139 <sup>(b)</sup>	-25.15	-24.34	-24.46	-24.61	0.89	1.14	2.78	16.46	No	No	Yes	E	V
PG2251+113	-27.66	-27.59	-24.64	-24.63	15.11	0.99	...	...	No	No	No	?	V
PG2349-014	-26.74	-26.20	-25.73	-25.78	1.54	1.05	...	...	No	No	Str	A	IVb

Col 1: Object name.

Col 2: Total absolute magnitude (host + PSF - companions).

Col 3: Absolute magnitude of PSF component.

Col 4: Absolute magnitude of host galaxy (including tidal features).

Col 5: Absolute magnitude of best-fitting galaxy host model.

Col 6: PSF-to-host intensity ratio.

Col 7: Model-to-host intensity ratio.

Col 8: Half-light radius in kpc of n=4 Sérsic component.

Col 9: Mean surface brightness of n=4 Sérsic component within half-light radius in H mag. arcsec<sup>-2</sup>.

Col 10: Presence of a stellar bar.

Col 11: Presence of spiral arms.

Col 12: Presence of merger-induced disturbance (Str=strongly disturbed).

Col 13: Morphological class: E = elliptical, B+D = bulge+disk, D = disk, A = ambiguous. Question marks (“?”) indicate uncertain classification due to PSF mismatch (see Sections 3 and 4.1).

Col 14: Interaction class (see VSK02 for details on the definitions).

<sup>(a)</sup> Entries in this table are the parameters from the best-fitting one or two galaxy component models (Tables 2 and 3).

<sup>(b)</sup> Entries for this object are uncertain because the host galaxy fills most of the field of view so the sky background is not well determined.

Table 6. Black Hole Mass

Galaxy (1)	$M_{BH}/10^7 M_{\odot}$				References (6)
	phot (2)	dyn (3)	rev (4)	vir (5)	
ULIRGs					
IRAS00091–0738	22.1	2.46	...	...	2 1 . .
IRAS00188–0856	26.6	...	...	...	3 . . .
IRAS00199–7426	...	2.95	...	...	. 4 . .
IRAS00262+4251	...	7.02	...	...	. 1 . .
IRAS00397–1312	31.5	1.05	...	...	3 1 . .
IRAS00456–2904SW	27.7	5.79	...	...	3 1 . .
IRAS00456–2904NE	2.1	...	...	...	3 . . .
IRAS00482–2721	10.6	...	...	...	2 . . .
IRAS01003–2238	7.61	2.54	...	...	3 1 . .
IRAS01166–0844	25.2	...	...	...	2 . . .
IRAS01166–0844NW	...	1.51	...	...	. 4 . .
IRAS01166–0844SE	...	4.97	...	...	. 4 . .
IRAS01199–2307SW	14.3	...	...	...	2 . . .
IRAS01199–2307NE	1.6	...	...	...	2 . . .
IRAS01298–0744	10.8	...	...	...	2 . . .
IRAS01355–1814	18.7	...	...	...	2 . . .
IRAS01388–4618	...	3.60	...	...	. 1 . .
IRAS01494–1845	44.8	...	...	...	2 . . .
IRAS01569–2939	24.9	...	...	...	2 . . .
PG0157+001	125.8	13.5	...	...	5 1 . .
IRAS02021–2103	46.8	3.50	...	...	3 1 . .
IRAS02364–4751N	...	8.32	...	...	. 4 . .
IRAS02364–4751S	...	4.36	...	...	. 4 . .
IRAS02411+0353	63.1	...	...	...	2 . . .
IRAS02480–3745	20.8	...	...	...	2 . . .
IRAS03209–0806	23.1	...	...	...	2 . . .
IRAS03250+1606	34.0	...	...	...	3 . . .
IRAS03521+0028	28.9	...	...	...	2 . . .
IRAS04074–2801	20.3	...	...	...	2 . . .
IRAS04103–2838	28.3	2.32	...	...	3 1 . .
IRAS04313–1649	21.4	5.10	...	...	3 1 . .
IRAS05020–2941	11.3	...	...	...	2 . . .
IRAS05024–1941	36.6	...	...	...	3 . . .
IRAS05156–3024	21.7	...	...	...	2 . . .
IRAS05189–2524	20.8	2.95	...	...	3 1 . .
IRAS06035–7102NE	...	2.04	...	...	. 4 . .
IRAS06035–7102SW	...	2.86	...	...	. 4 . .
IRAS07598+6508	39.0	...	...	...	3 . . .
IRAS08201+2801	35.1	...	...	...	2 . . .
IRAS08474+1813	5.7	...	...	...	2 . . .
IRAS08559+1053	71.7	...	...	...	2 . . .

Table 6—Continued

Galaxy (1)	$M_{BH}/10^7 M_{\odot}$				References (6)
	phot (2)	dyn (3)	rev (4)	vir (5)	
IRAS08572+3915	9.0	...	...	...	2 . . .
IRAS08591+5248	37.0	...	...	...	2 . . .
IRAS09039+0503	22.9	9.45	...	...	3 1 . .
IRAS09111–1007E	5.0	...	...	...	. 1 . .
IRAS09111–1007W	66.6	1.31	...	...	. 1 . .
IRAS09116+0334	97.8	...	...	...	2 . . .
IRAS09463+8141	30.8	...	...	...	2 . . .
IRAS09539+0857	6.84	...	...	...	3 . . .
IRAS10035+2740	55.5	...	...	...	2 . . .
IRAS10091+4704	42.5	...	...	...	2 . . .
IRAS10190+1322	70.2	...	...	...	2 . . .
IRAS10190+1322NE	...	6.86	...	...	. 4 . .
IRAS10190+1322SW	...	2.18	...	...	. 4 . .
IRAS10378+1109	19.7	...	...	...	2 . . .
IRAS10485–1447E	2.5	...	...	...	2 . . .
IRAS10485–1447W	8.7	...	...	...	2 . . .
IRAS10494+4424	14.6	...	...	...	2 . . .
IRAS10565+2448	...	2.04	...	...	. 4 . .
IRAS10594+3818	52.1	...	...	...	2 . . .
IRAS11028+3130	11.2	...	...	...	2 . . .
IRAS11095–0238	7.53	...	...	...	3 . . .
IRAS11095–0238NE	...	3.92	...	...	. 4 . .
IRAS11095–0238SW	...	2.95	...	...	. 4 . .
IRAS11119+3257	278.6	...	...	...	2 . . .
IRAS11130–2659	15.1	...	...	...	2 . . .
IRAS11180+1623E	14.4	...	...	...	2 . . .
IRAS11180+1623W	4.3	...	...	...	2 . . .
IRAS11223–1244E	28.0	...	...	...	2 . . .
IRAS11223–1244W	53.2	4.13	...	...	2 1 . .
IRAS11387+4116	30.2	...	...	...	2 . . .
IRAS11506+1331	21.0	...	...	...	3 . . .
IRAS11582+3020	24.9	...	...	...	2 . . .
IRAS11598–0112	43.9	...	...	...	2 . . .
IRAS12018+1941	30.2	...	...	...	2 . . .
IRAS12032+1707	65.9	...	...	...	2 . . .
IRAS12072–0444	27.4	...	...	...	3 . . .
IRAS12072–0444N	...	2.39	...	...	. 4 . .
IRAS12072–0444S	...	3.50	...	...	. 4 . .
IRAS12112+0305	20.8	...	...	...	2 . . .
IRAS12112+0305NE	...	1.98	...	...	. 4 . .
IRAS12112+0305SW	...	2.62	...	...	. 4 . .
IRAS12127–1412NE	53.2	...	...	...	2 . . .
IRAS12127–1412SW	0.8	...	...	...	2 . . .
3C273	1082.0	...	88.6	...	2 . 6 .

Table 6—Continued

Galaxy (1)	$M_{BH}/10^7 M_{\odot}$				References (6)
	phot (2)	dyn (3)	rev (4)	vir (5)	
IRAS12359–0725N	8.5	...	...	...	2 . . .
IRAS12359–0725S	4.4	...	...	...	2 . . .
IRAS12447+3721	13.4	...	...	...	2 . . .
Mrk231	37.8	1.73	...	...	3 1 . .
IRAS13106–0922	14.8	...	...	...	2 . . .
IRAS13218+0552	35.8	...	...	...	3 . . .
IRAS13305–1739	68.0	...	...	...	2 . . .
IRAS13335–2612	22.9	...	...	...	2 . . .
IRAS13335–2612N	...	3.22	...	...	. 4 . .
IRAS13335–2612S	...	7.89	...	...	. 4 . .
IRAS13342+3932	130.5	...	...	...	2 . . .
Mrk273	19.9	56.1	...	...	2 1 . .
IRAS13443+0802NE	117.3	...	...	...	2 . . .
IRAS13443+0802SW	6.6	...	...	...	2 . . .
IRAS13451+1232	71.7	...	...	...	2 . . .
IRAS13451+1232E	...	3.81	...	...	. 4 . .
IRAS13451+1232W	...	6.54	...	...	. 4 . .
IRAS13454–2956N	34.3	...	...	...	2 . . .
IRAS13454–2956S	46.3	...	...	...	2 . . .
IRAS13469+5833	50.4	...	...	...	2 . . .
IRAS13509+0442	31.5	...	...	...	2 . . .
IRAS13539+2920	44.3	...	...	...	2 . . .
IRAS14053–1958	19.3	...	...	...	2 . . .
IRAS14060+2919	54.3	...	...	...	2 . . .
IRAS14070+0525	42.0	3.13	...	...	3 1 . .
IRAS14121–0126	48.8	...	...	...	2 . . .
IRAS14197+0813	21.9	...	...	...	3 . . .
IRAS14202+2615	102.0	...	...	...	2 . . .
IRAS14252–1550	27.7	...	...	...	2 . . .
IRAS14348–1447	40.7	...	...	...	2 . . .
IRAS14348–1447NE	...	7.02	...	...	. 1 . .
IRAS14348–1447SW	...	4.25	...	...	. 1 . .
IRAS14378–3651	...	4.60	...	...	. 1 . .
IRAS14394+5332E	36.2	...	...	...	2 . . .
IRAS14394+5332W	10.9	...	...	...	2 . . .
IRAS14485–2434	19.5	...	...	...	2 . . .
IRAS15001+1433E	55.5	...	...	...	2 . . .
IRAS15043+5754	88.8	...	...	...	2 . . .
IRAS15130–1958	14.4	8.26	...	...	3 1 . .
IRAS15206+3342	35.8	...	...	...	2 . . .
IRAS15225+2350	21.7	...	...	...	2 . . .
IRAS15250+3609	...	4.25	...	...	. 1 . .
Arp220	15.1	6.08	...	...	2 1 . .
IRAS15462–0450	11.4	6.86	...	...	3 1 . .

Table 6—Continued

Galaxy (1)	$M_{BH}/10^7 M_{\odot}$				References (6)
	phot (2)	dyn (3)	rev (4)	vir (5)	
IRAS16090–0139	37.0	...	...	...	2 . . .
IRAS16156+0146	8.8	...	...	...	2 . . .
IRAS16156+0146NW	...	10.8	...	...	. 4 . .
IRAS16156+0146SE	...	0.521	...	...	. 4 . .
IRAS16300+1558	60.5	3.31	...	...	3 4 . .
IRAS16334+4630	44.3	...	...	...	2 . . .
IRAS16468+5200	13.7	...	...	...	2 . . .
IRAS16474+3430	62.4	...	...	...	2 . . .
IRAS16487+5447	20.3	...	...	...	2 . . .
NGC6240	...	23.3	...	...	. 1 . .
IRAS17028+5817E	12.3	...	...	...	2 . . .
IRAS17028+5817W	19.1	...	...	...	2 . . .
IRAS17044+6720	12.4	...	...	...	2 . . .
IRAS17068+4027E	35.1	...	...	...	2 . . .
IRAS17179+5444	29.9	...	...	...	2 . . .
IRAS17208–0014	...	23.3	...	...	. 1 . .
IRAS19254–7245N	...	1.73	...	...	. 4 . .
IRAS19254–7245S	...	7.89	...	...	. 4 . .
IRAS20046–0623W	...	3.71	...	...	. 4 . .
IRAS20087–0308	...	19.4	...	...	. 1 . .
IRAS20414–1651	10.7	10.3	...	...	3 1 . .
IRAS20551–4250	...	3.22	...	...	. 1 . .
IRAS21130–4446NE	...	6.23	...	...	. 4 . .
IRAS21130–4446SW	...	4.48	...	...	. 4 . .
IRAS21208–0519	86.9	...	...	...	2 . . .
IRAS21208–0519N	...	2.12	...	...	. 4 . .
IRAS21208–0519S	...	7.19	...	...	. 4 . .
IRAS21219–1757	40.7	1.79	...	...	3 1 . .
IRAS21329–2346	14.4	...	...	...	3 . . .
IRAS21329–2346N	...	1.46	...	...	. 4 . .
IRAS21329–2346S	...	1.36	...	...	. 4 . .
IRAS21477+0502E	26.6	...	...	...	2 . . .
IRAS21477+0502W	5.2	...	...	...	2 . . .
IRAS21504–0628	...	0.545	...	...	. 1 . .
IRAS22088–1831	54.3	...	...	...	2 . . .
IRAS22206–2715	54.3	...	...	...	2 . . .
IRAS22491–1808	27.1	...	...	...	2 . . .
IRAS22491–1808E	...	3.81	...	...	. 4 . .
IRAS22491–1808W	...	1.79	...	...	. 4 . .
IRAS22541+0833NW	27.1	...	...	...	2 . . .
IRAS22541+0833SE	6.1	...	...	...	2 . . .
IRAS23060+0505	38.6	...	...	...	2 . . .
IRAS23128–5919N	...	4.36	...	...	. 4 . .
IRAS23128–5919S	...	4.02	...	...	. 4 . .

Table 6—Continued

Galaxy (1)	$M_{BH}/10^7 M_{\odot}$				References (6)
	phot (2)	dyn (3)	rev (4)	vir (5)	
IRAS23129+2548	20.1	...	...	...	2 . . .
IRAS23230–6926	...	3.50	...	...	. 1 . .
IRAS23233+2817	25.2	...	...	...	2 . . .
IRAS23234+0946	37.0	...	...	...	2 . . .
IRAS23234+0946N	...	4.48	...	...	. 4 . .
IRAS23234+0946S	...	1.36	...	...	. 4 . .
IRAS23327+2913N	10.6	...	...	...	2 . . .
IRAS23327+2913S	18.5	...	...	...	2 . . .
IRAS23365+3604	...	3.71	...	...	1 . . .
IRAS23389+0300	16.6	...	...	...	2 . . .
IRAS23498+2423	165.0	...	...	...	2 . . .
IRAS23578–5307	...	11.0	...	...	. 1 . .
PG QSOs					
PG0003+199	...	...	1.42	186.2	. . 6 8
PG0007+106	24.4	13.8	...	53.5	5 7 . 8
PG0026+129	27.1	...	39.3	...	5 . 6 .
PG0050+124	34.3	10.5	...	2.76	5 7 . 8
PG0804+761	...	...	69.3	...	. . 6 .
PG0838+770	11.4	...	...	14.3	5 . . 8
PG0844+349	5.4	...	9.24	...	5 . 6 .
PG0923+201	47.8	...	...	10.2	5 . . 8
PG0953+414	...	...	27.6	...	. . 6 .
PG1001+054	12.6	...	...	5.47	5 . . 8
PG1116+215	18.3	...	...	33.8	5 . . 8
PG1119+120	8.4	5.79	...	2.95	5 7 . 8
PG1126–041	7.4	11.9	...	5.61	5 7 . 8
PG1211+143	...	...	14.6	9.14	. . 6 8
PG1229+204	28.0	5.79	7.32	...	5 7 6 .
PG1302–102	69.5	...	...	75.7	5 . . 8
PG1307+085	21.0	...	44.0	...	5 . 6 .
PG1309+355	94.7	...	...	22.1	5 . . 8
PG1404+226	...	26.7	...	0.77	. 7 . 8
PG1411+442	24.9	...	44.3	...	5 . 6 .
PG1426+015	23.4	9.87	129.8	...	5 7 6 .
PG1435–067	10.2	...	...	23.2	5 . . 8
PG1440+356	25.2	...	...	2.94	5 . . 8
PG1613+658	130.5	...	27.9	...	5 . 6 .
PG1617+175	9.1	9.45	59.4	...	5 7 6 .
PG1626+554	24.6	...	...	31.5	5 . . 8
PG1700+518	106.5	...	78.1	...	5 . 6 .
PG2130+099	25.2	7.36	45.7	...	5 7 6 .
PG2214+139	11.2	4.97	...	35.6	5 7 . 8

Table 6—Continued

Galaxy (1)	$M_{BH}/10^7 M_{\odot}$				References (6)
	phot (2)	dyn (3)	rev (4)	vir (5)	
B2 2201+31A	200.0	...	...	...	5 . . .
PG2251+113	43.0	...	...	97.5	5 . . 8
PG2349–014	137.6	...	...	...	5 . . .

References. — 1 = Dasyra et al. 2006b; 2 = Veilleux et al. 2002; 3 = Veilleux et al. 2006; 4 = Dasyra et al. 2006a; 5 = This paper; 6 = Peterson et al. 2004; 7 = Dasyra et al. 2007; 8 = Vestergaard & Peterson, 2006

Note. — Col.(1): Galaxy name. Col.(2-5): Black hole mass, in units of  $10^7 M_{\odot}$ , as determined from spheroid luminosity, spheroid velocity dispersion, reverberation mapping, and virial relation. Col.(6):  $M_{BH}$  references.

Table 7. Black Hole Mass Statistics

Quantity (1)	$\log(M_{BH}/10^7 M_\odot)$			
	phot (2)	dyn (3)	rev (4)	vir (5)
ULIRGs				
No. Gals.	134	72	1	0
Average	42.85	5.76	88.60	...
Median	26.90	3.76	88.60	...
Std. Dev.	96.84	7.49	88.60	...
PG QSOs				
No. Gals.	27	10	14	18
Average	43.77	10.61	42.71	34.07
Median	24.90	9.66	41.70	18.20
Std. Dev.	48.59	6.34	34.15	46.52
ULIRGs + PG QSOs				
No. Gals.	161	82	15	18
Average	43.01	6.35	45.77	34.07
Median	25.20	4.19	44.00	18.20
Std. Dev.	90.43	7.50	34.98	46.52

Note. — Col.(1): Quantity. Col.(2 – 5): Black hole mass statistics, where individual  $M_{BH}$  values are first divided by  $10^7 M_\odot$  and then logged. Masses are determined from spheroid luminosity, spheroid velocity dispersion, reverberation mapping, and virial relation.



Fig. 1.— Results from the GALFIT one galaxy component analysis. For each object, panel (a) shows the original data while the other panels show the residuals after subtracting three different models: (b) PSF + Sérsic component with  $n = 1$  (exponential disk), (c) PSF + Sérsic component with  $n = 4$  (de Vaucouleurs spheroid), and (d) PSF + Sérsic component with unconstrained index. The intensity scale is logarithmic and the horizontal segment between panels (b) and (c) represents 10 kpc. The tickmarks in the panels are separated by  $5''$ .

Fig. 2.— Results from the GALFIT two galaxy component analysis for 16 PG QSOs with possible low-surface-brightness exponential disks. A disk is detected unambiguously in 9 of these objects: PG 0050+124, 0838+770, 0844+349, 1119+120, 1126-041, 1229+204, 1426+015, 1440+356, and 2130+099 (see details in Table 5). In the other systems presented here, the addition of a disk component did not improve the fits significantly. Panel (a) shows the original data and panel (b) shows the residuals after subtracting a model with a PSF, a bulge-like Sérsic component with  $n = 4$ , and a disk-like Sérsic component with  $n = 1$ . Panels (c) and (d) show the surface brightness distributions of the two Sérsic components used in the model. The centroids of the components are left unconstrained. The intensity scale is logarithmic and the vertical segment between panels (b) and (c) represents 10 kpc. The tickmarks in each panel are separated by  $5''$ .

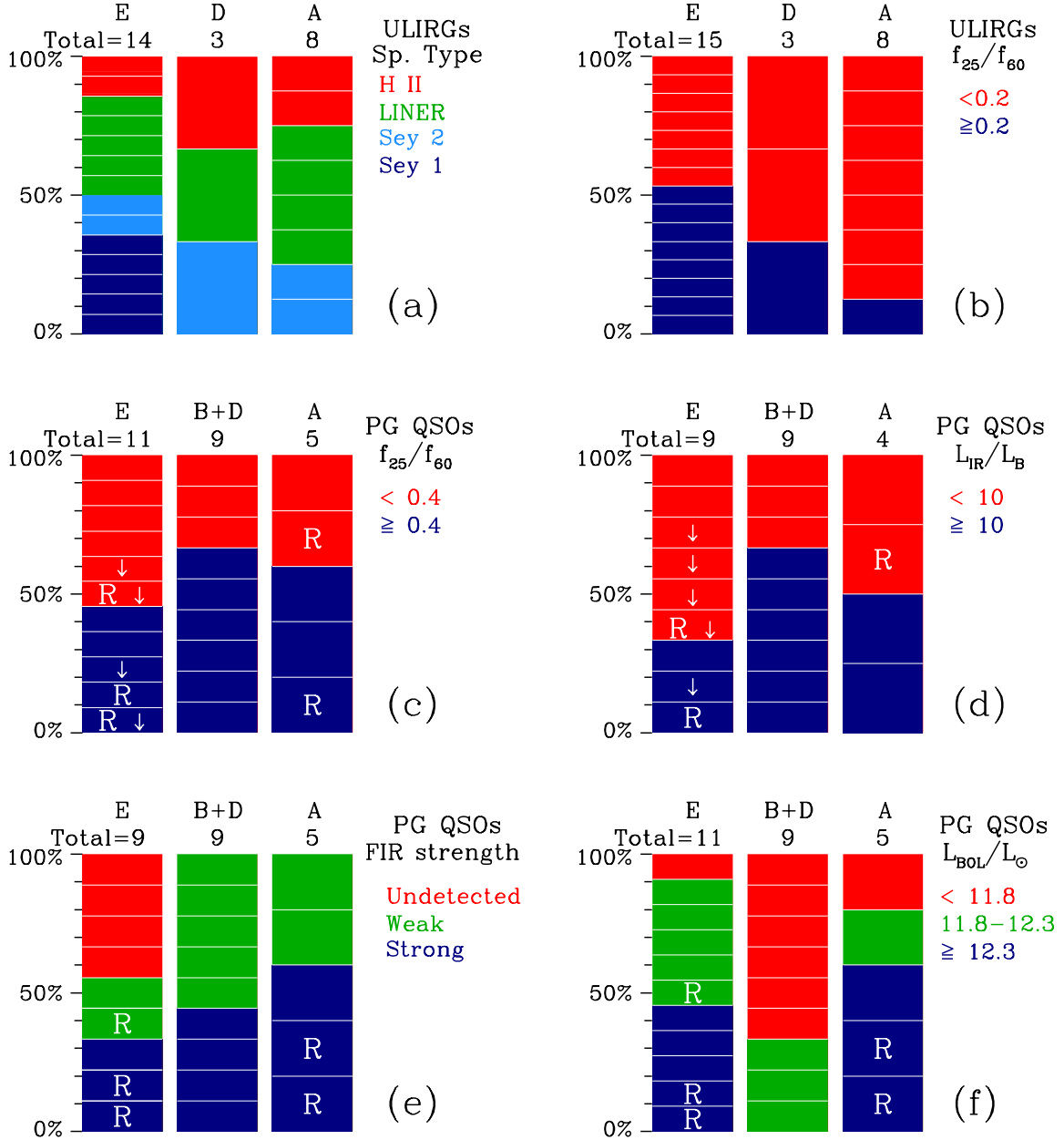


Fig. 3.— Trends between morphological types (E = elliptical, D = disk, B+D = bulge + disk, and A = ambiguous) and (a) optical spectral types among the ULIRGs from Paper I, (b) *IRAS* 25-to-60  $\mu\text{m}$  colors among the ULIRGs from Paper I, (c) *IRAS* 25-to-60  $\mu\text{m}$  colors among PG QSOs, (d) infrared excess,  $L_{\text{IR}}/L_{\text{B}}$  among PG QSOs, (e) FIR strength,  $L(60 \mu\text{m})/L(15 \mu\text{m})$ , among PG QSOs, and (f) bolometric luminosity among PG QSOs. Radio-loud PG QSOs are indicated by an “R”. Panels (a) and (b) show that the hosts of warm, quasar-like ULIRGs all have a prominent spheroidal component, while the other panels indicate that QSOs with small infrared excesses, undetected FIR emission, and high bolometric luminosities favor elliptical hosts. Radio-loud QSOs avoid late-type systems with disks.

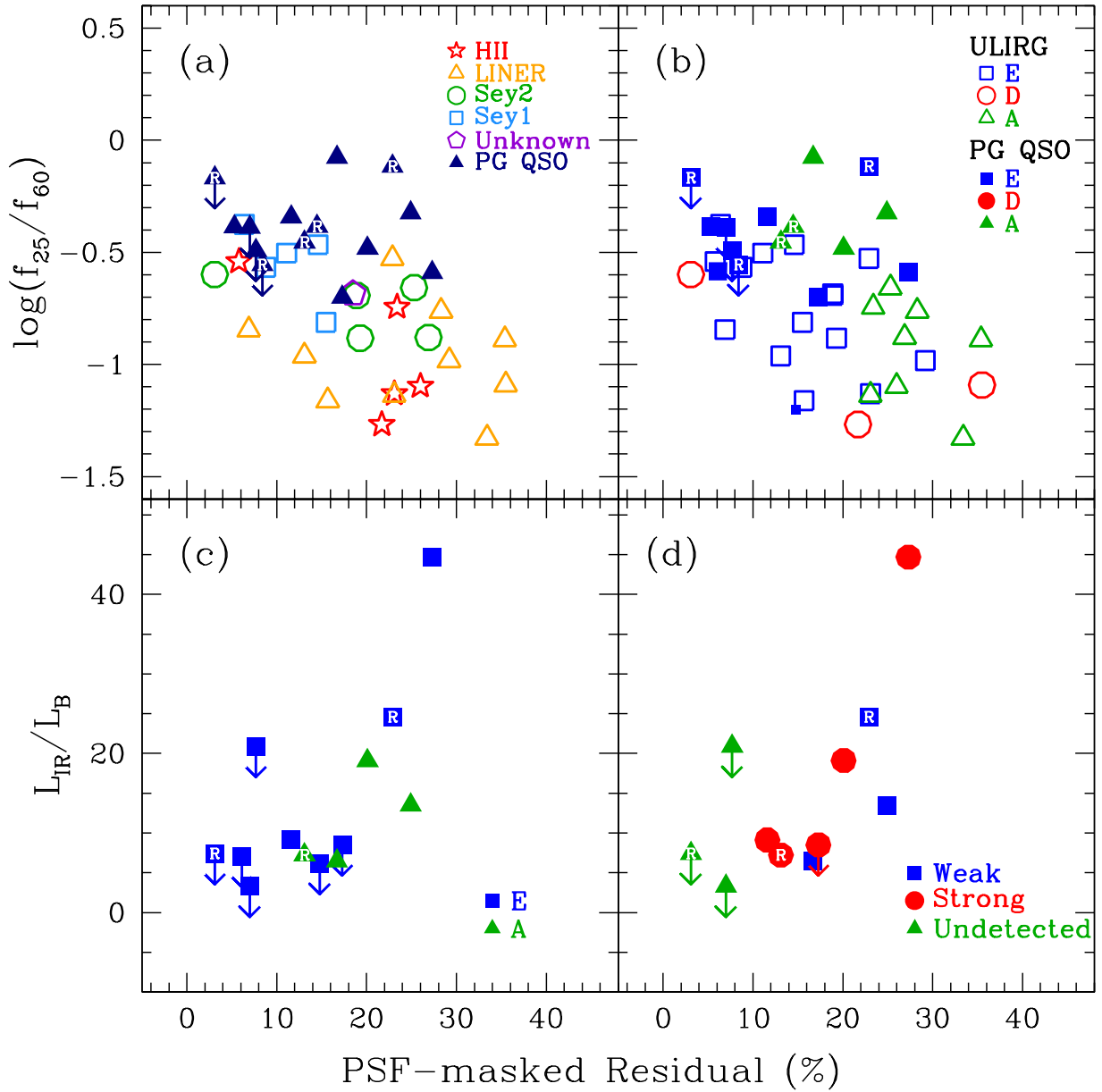


Fig. 4.— The PSF-masked residuals (as defined in the text) plotted against (a) and (b) the *IRAS* 25-to-60  $\mu\text{m}$  colors and (c) and (d) the infrared excesses. The top panels contain all ULIRGs and PG QSOs in our study while the bottom two panels show only the PG QSOs. The data are labeled either by optical spectral type, morphological class, or FIR strength. Radio-loud PG QSOs are indicated by an “R”. The residuals for the 9 QSOs that are bulge + disk systems (B + D) are not shown in these panels since the residuals from the two galaxy component fits are necessarily smaller than those from the one galaxy component fits. The residuals are smaller among warm, quasar-like ULIRGs and QSOs (a) with dominant elliptical morphology (b), small infrared excesses (c) and undetected FIR emission (d).

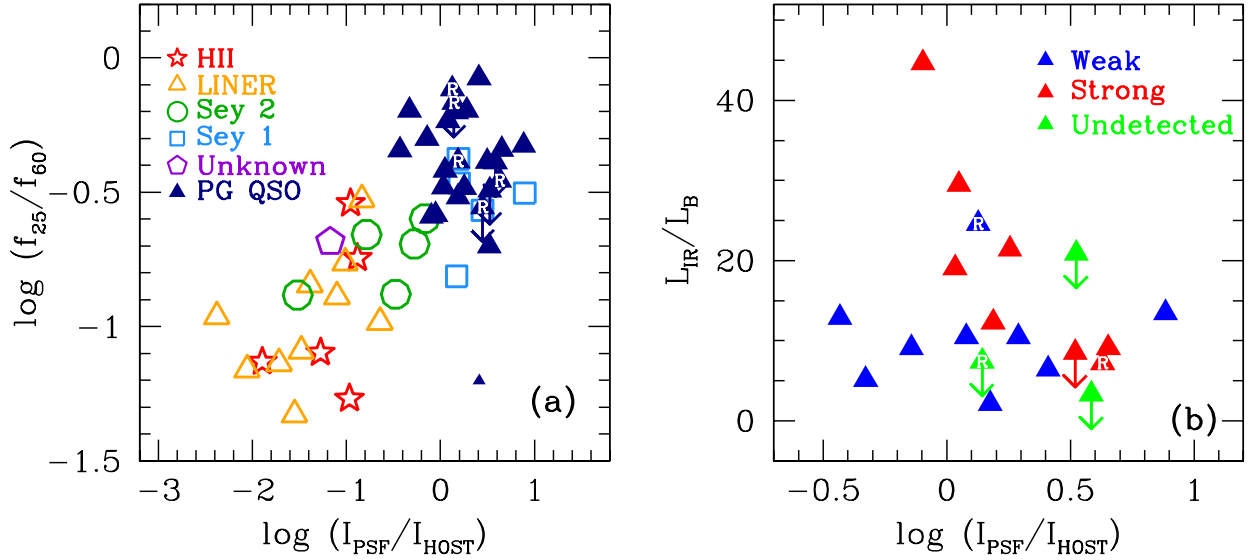


Fig. 5.— The intensity of the PSF component normalized to that of the host galaxy,  $I_{PSF}/I_{host}$ , is plotted against (a) the *IRAS* 25-to-60  $\mu\text{m}$  colors of ULIRGs and PG QSOs and (b) the infrared excess,  $L_{IR}/L_B$ , of PG QSOs only. The data are labeled either by optical spectral type (a) or FIR strength (b). Radio-loud PG QSOs are indicated by an “R”. Warm, quasar-like ULIRGs and PG QSOs have stronger PSF components than H II and LINER ULIRGs. Infrared-excess QSOs tend to have weaker PSF components than infrared-faint QSOs on average, although significant scatter is seen.

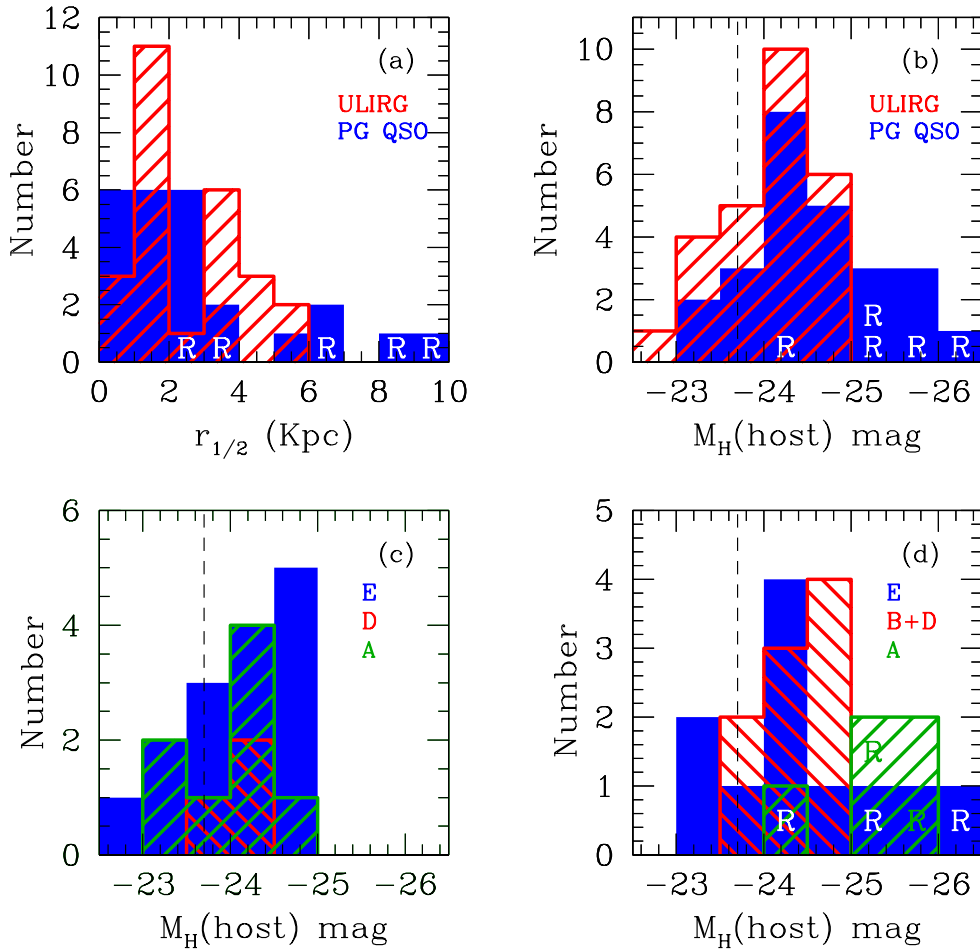


Fig. 6.— Distribution of the half-light radii (spheroid component only) and total host (spheroid + disk + tidal features, if relevant) absolute magnitudes for all ULIRGs and PG QSOs in the *HST* sample. Radio-loud PG QSOs are indicated by an “R”. The vertical dashed line in panels (b), (c), and (d) represents  $M_H^* = -23.7$  mags, the H-band absolute magnitude of a  $L^*$  galaxy in a Schechter function description of the local field galaxy luminosity function. In panels (a) and (b), the ULIRGs are cross-hatched red and the PG QSOs are in blue. A K-S test on these data indicates no significant difference between the host sizes and magnitudes of the 1-Jy ULIRGs and radio-quiet PG QSOs in this sample. The radio-loud QSOs are, however, significantly larger and brighter than the ULIRGs and radio-quiet QSOs. Panel (c) shows the distribution of host absolute magnitudes for ULIRGs according to their morphology (blue represents elliptical, red hatched corresponds to late type, and green hatched indicates ambiguous systems). Panel (d) is the same as panel (c) but for the PG QSOs. No obvious trends with dominant morphological type are seen in the ULIRG data. QSOs with elliptical hosts show a broad range of host absolute magnitude, while QSOs with bulge + disk and ambiguous morphology tend to populate the lower and upper ends of the host luminosity distribution, respectively.

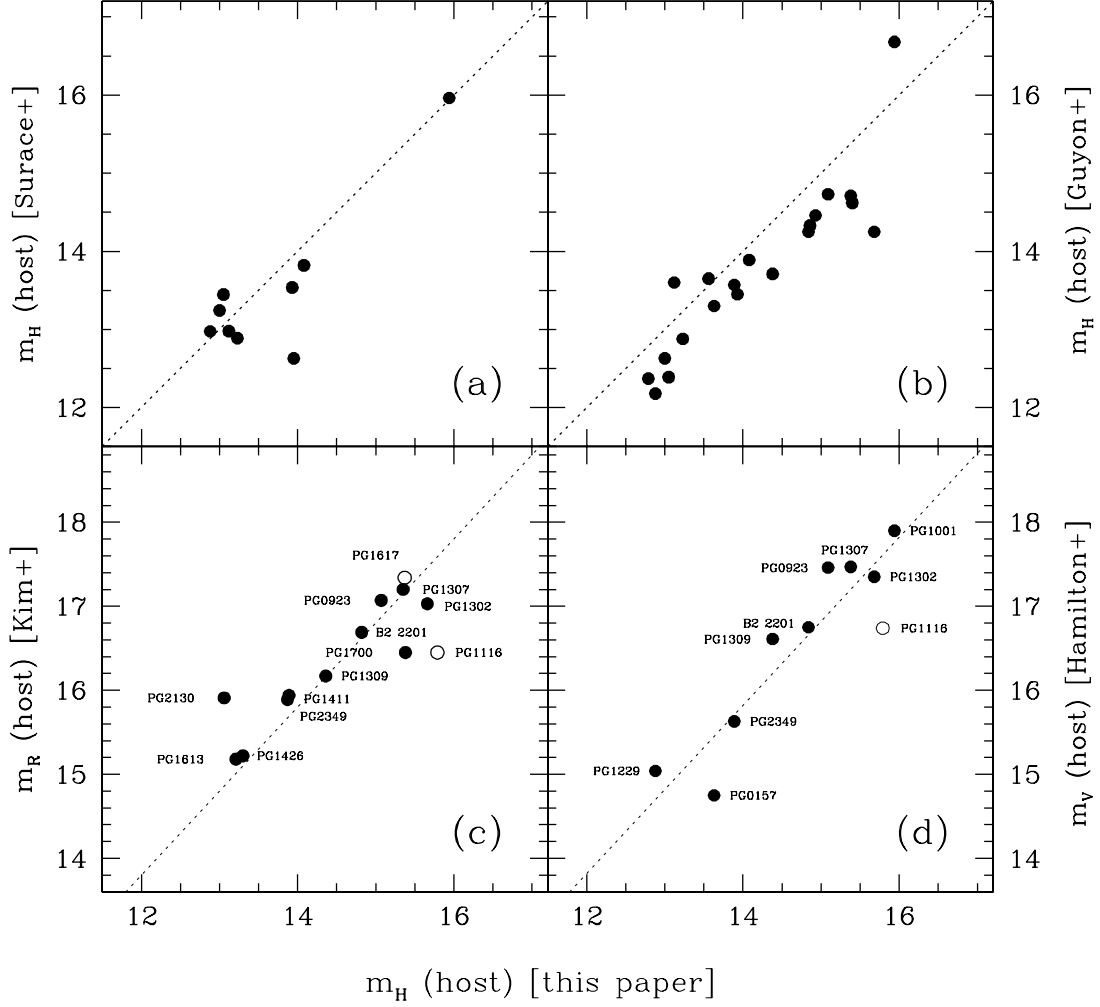


Fig. 7.— Comparison of the host magnitudes derived from our *HST* data with the results derived from (a) tip-tilt H-band imaging by Surace et al. (2001), (b) adaptive optics H-band imaging by Guyon et al. (2006), (c) archived *HST* R-band imaging of Kim et al. (2008), and (d) archived *HST* V-band imaging of Hamilton et al. (2008). An excellent match is found with the data of Surace et al., except for one object, PG 0007+106 (open circle in a). This is an optically violently variable source so the difference may be due to uncertainties in the removal of the central PSF in Surace et al. data. The Guyon et al. values are systematically  $\sim 0.4$  mag. brighter than our measurements. Given the good agreement between our data and those of Surace et al., we suspect that this shift is either due to uncertainties in the PSF subtraction from the AO data of Guyon et al. or systematic underestimate of their background level. The median R–H color (V–H) of the 13 (10) QSOs in c (d) is 1.9 (1.9) mag. and is shown as the dashed diagonal line. The symbols in these two panels indicate the reliability of the H-band host magnitudes (filled circle = reliable, open circles = less reliable due to PSF mismatch; these data points were not used in the calculations of the averages).

Fig. 8.— H-band FP of elliptical galaxies. In both panels, the large solid symbols are ULIRGs and PG QSOs with “pure” elliptical ( $n = 4$ ) hosts from the present NICMOS sample. The bulges of the bulge + disk systems are excluded to avoid uncertainties related to the bulge/disk decomposition. The open symbols are the optical mergers of Rothberg & Joseph (2006; purple stars) and the optically/X-ray/radio more luminous QSOs from Dunlop et al. (2003; brown diamonds), Hamilton et al. (2008; green squares), and Wolf & Sheinis (2008; red triangles). The small dots represent the data from Pahre (1999; blue), Bernardi et al. (2003; orange), and Zibetti et al. (2002; cyan) on inactive spheroids. See text for assumed color transformation. Radio-loud PG QSOs are indicated by an “R”. The dotted line is a linear fit through the data on inactive spheroids, the solid line is a linear fit through the NICMOS data on the PG QSOs, and the short-dashed line is a linear fit through the ULIRGs. The slope of the relation for ULIRGs is indistinguishable from that of the QSOs but is significantly steeper than for inactive spheroids. A systematic shift at small half-light radii is also seen in panel (b), where the stellar velocity dispersions on the ULIRGs and PG QSOs from Dasyra et al. (2006b, 2007) are compared with the FP of inactive spheroids. This trend is also seen among the optical mergers of Rothberg & Joseph (2006).

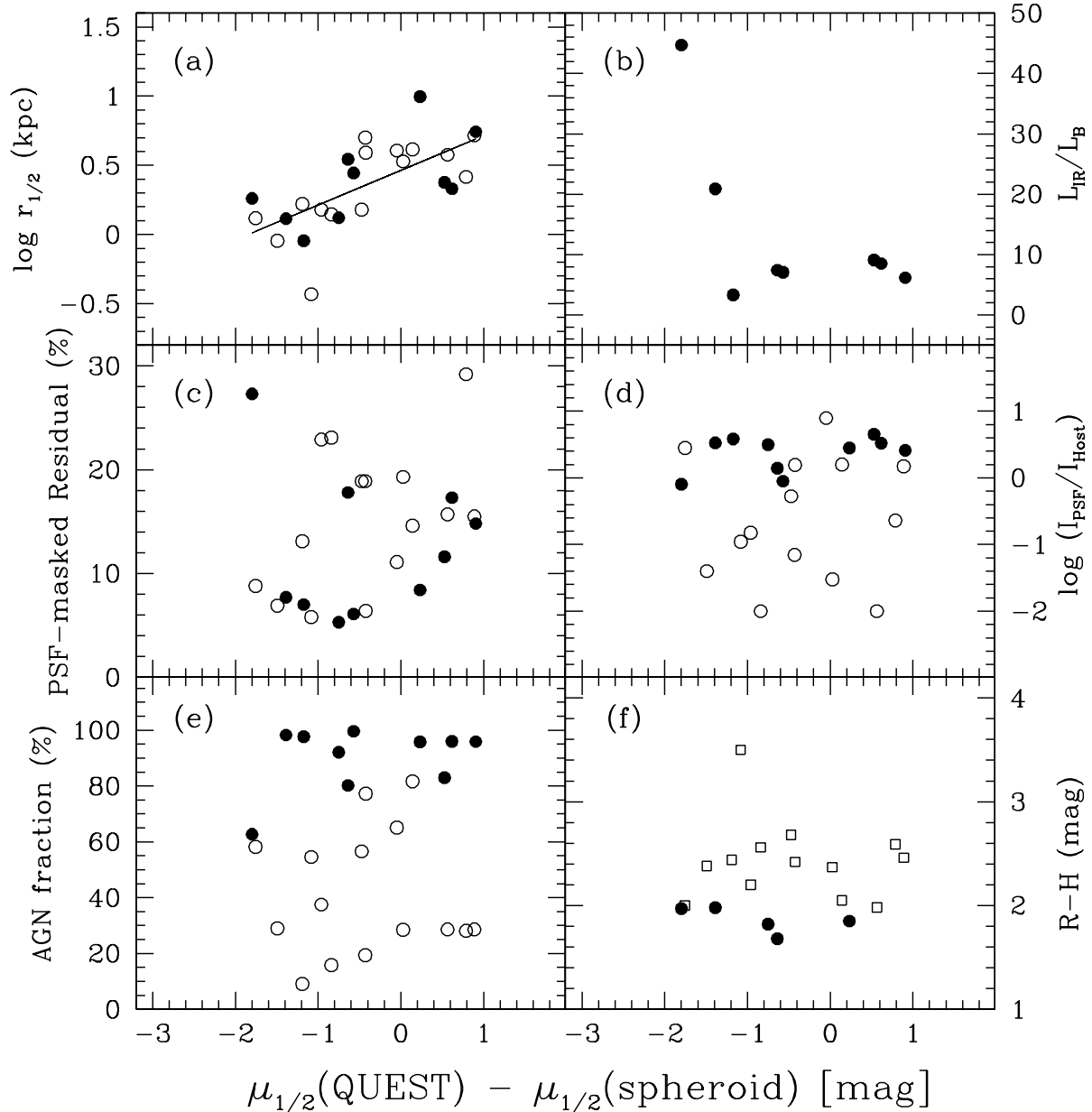


Fig. 9.— Surface brightness deviation as a function of (a) half-light radius, (b) infrared excess, (c) PSF-masked residual, (d) PSF-host flux ratio, (e) *Spitzer*-derived AGN fractional contribution to the bolometric luminosity (from Veilleux et al. 2009), and (f) R–H host colors for the ULIRGs from Veilleux et al. (2002; open squares), Veilleux et al. (2006; open circles), and PG QSOs of this paper (filled circles). The surface brightness excess is defined as the difference between the observed surface brightness and the surface brightness expected of an inactive spheroidal galaxy with the same half-light radius, as determined by a linear regression through the data of Pahre (1999) or Bernardi et al. (2003) in Figure 8a. The bulges of the bulge + disk systems are excluded to avoid uncertainties related to the bulge/disk decomposition. An obvious trend is seen with galaxy size (the probability that this correlation is fortuitous  $P[\text{null}] = 0.02\%$ ) and perhaps also with infrared excess though the statistics for this latter quantity are poor.



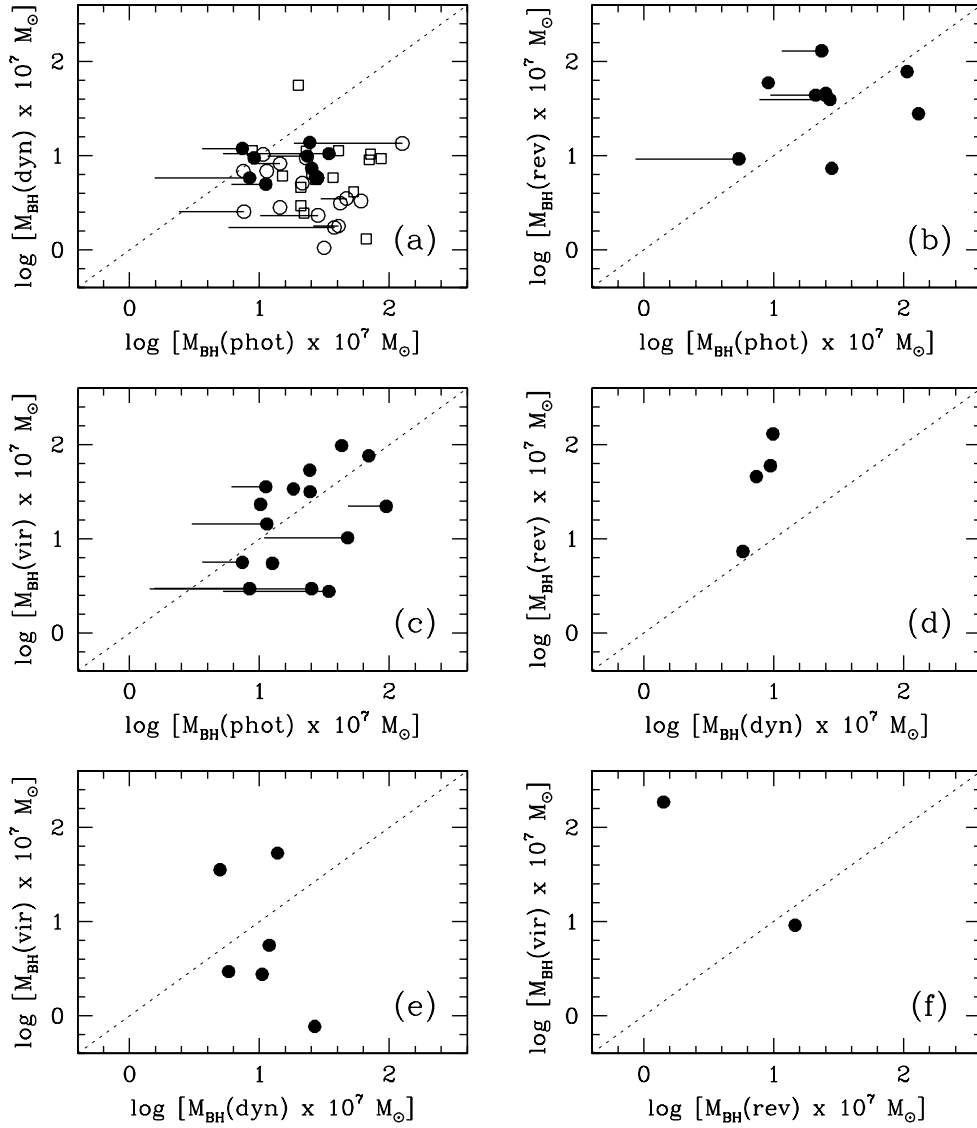


Fig. 10.— Comparison of black hole masses in ULIRGs and PG QSOs derived from the photometric measurements of Paper I and the present paper, the stellar dynamical measurements of Dasyra et al. (2006a, 2006b, 2007), the reverberation mapping measurements of Peterson et al. (2004) updated by Bentz et al. (2006), and the virial masses of Vestergaard & Peterson (2006). ULIRGs from Veilleux et al. (2002) are the open squares, ULIRGs from Veilleux et al. (2006) are the open circles, and PG QSOs of this paper are the filled circles. Systems with either “pure” elliptical or bulge + disk hosts are included here. Discrepancies are seen in all panels, particularly those involving the dynamical measurements of large black hole masses. The best agreement (to within a factor of 3) is seen when comparing the photometric, reverberation-mapping, and virial mass estimates (panels *b* and *c*). Horizontal segments on the photometric mass estimates indicate the effect of correcting the host magnitudes for possible excess H-band emission from a young circumnuclear stellar population (using the surface brightness deviations presented in Figure 9).

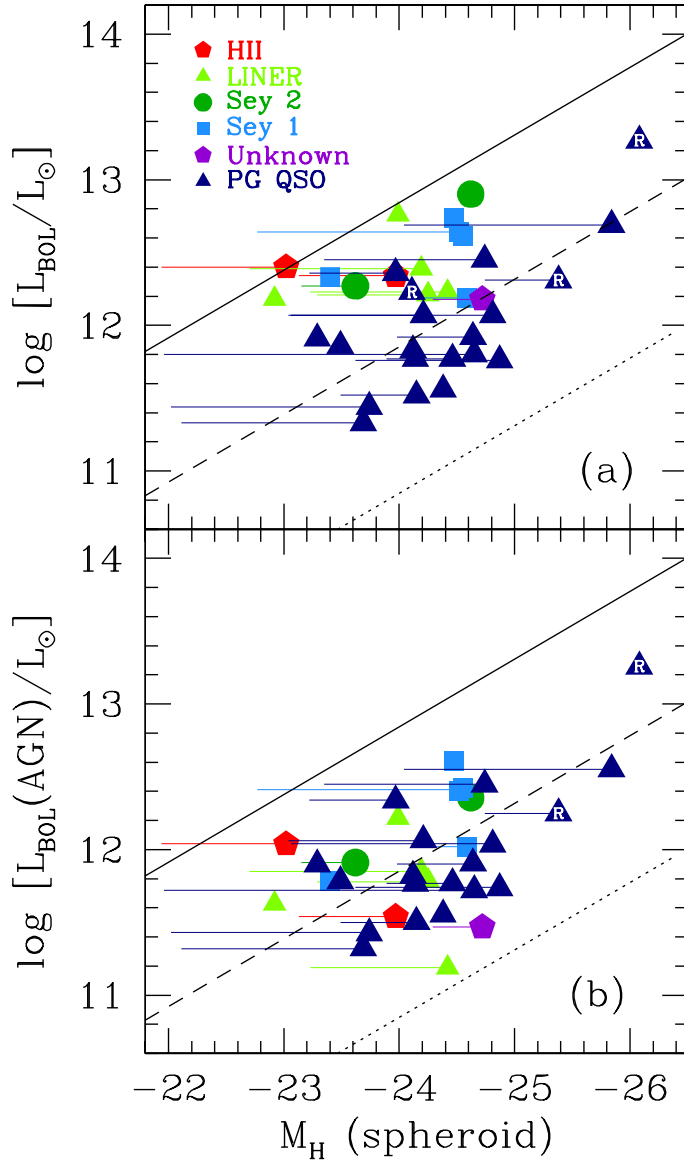


Fig. 11.— (a) Total bolometric luminosities and (b) AGN-only bolometric luminosities in ULIRGs and PG QSOs with elliptical hosts *versus* absolute H-band magnitudes of the spheroidal components derived from the NICMOS data. Radio-loud PG QSOs are indicated by an “R”. Systems with either “pure” elliptical or bulge + disk hosts are included here. Diagonal dotted, dashed, and solid lines represent 1%, 10%, 100% of the Eddington luminosity using the relation of Marconi & Hunt (2003) to translate spheroid magnitudes into black hole masses. The AGN fractional contributions to the bolometric luminosities used to produce panel (b) were taken from Veilleux et al. (2009). None of the objects in the sample radiate at super-Eddington rates. The Eddington ratios of the radio-quiet and radio-loud QSOs are statistically the same as those of ULIRGs on average (of order 3-30%). Horizontal segments on the spheroid magnitudes indicate the effect of correcting for possible excess H-band emission from a young circumnuclear stellar population (using the surface brightness deviations presented in Figure 9).

This figure "fig1a.jpg" is available in "jpg" format from:

<http://arxiv.org/ps/0906.3157v1>

This figure "fig1b.jpg" is available in "jpg" format from:

<http://arxiv.org/ps/0906.3157v1>

This figure "fig1c.jpg" is available in "jpg" format from:

<http://arxiv.org/ps/0906.3157v1>

This figure "fig1d.jpg" is available in "jpg" format from:

<http://arxiv.org/ps/0906.3157v1>

This figure "fig1e.jpg" is available in "jpg" format from:

<http://arxiv.org/ps/0906.3157v1>

This figure "fig1f.jpg" is available in "jpg" format from:

<http://arxiv.org/ps/0906.3157v1>



This figure "fig1g.jpg" is available in "jpg" format from:

<http://arxiv.org/ps/0906.3157v1>

This figure "fig2a.jpg" is available in "jpg" format from:

<http://arxiv.org/ps/0906.3157v1>

This figure "fig2b.jpg" is available in "jpg" format from:

<http://arxiv.org/ps/0906.3157v1>

This figure "fig2c.jpg" is available in "jpg" format from:

<http://arxiv.org/ps/0906.3157v1>

This figure "fig2d.jpg" is available in "jpg" format from:

<http://arxiv.org/ps/0906.3157v1>

This figure "fig8.jpg" is available in "jpg" format from:

<http://arxiv.org/ps/0906.3157v1>